THE GEOLOGICAL SOCIETY OF AMERICA®

Dating metasomatic events in the lithospheric mantle beneath the Calatrava volcanic field (central Spain)

Carlos Villaseca[1,*], Elena A. Belousova[2], Dan N. Barfod[3], and José M. González-Jiménez[4]

[1]DEPARTAMENTO DE MINERALOGÍA Y PETROLOGÍA, FACULTAD DE GEOLOGÍA, UNIVERSIDAD COMPLUTENSE (UCM), C/JOSÉ ANTONIO NOVAIS, 12. INSTITUTO DE GEOCIENCIAS (UCM, CSIC), 28040 MADRID, SPAIN

[2]ARC NATIONAL KEY CENTRE FOR GEOCHEMICAL EVOLUTION AND METALLOGENY OF CONTINENTS (GEMOC), DEPARTMENT OF EARTH AND PLANETARY SCIENCES, MACQUARIE UNIVERSITY, NORTH RYDE, NSW 2109, AUSTRALIA

[3]NATURAL ENVIRONMENT RESEARCH COUNCIL (NERC) ARGON ISOTOPE FACILITY, SCOTTISH UNIVERSITIES ENVIRONMENTAL RESEARCH CENTRE, RANKINE AVENUE, SCOTTISH ENTERPRISE TECHNOLOGY PARK, EAST KILBRIDE, G75 0QF, UK

[4]DEPARTAMENTO DE MINERALOGÍA Y PETROLOGÍA, FACULTAD DE CIENCIAS, UNIVERSIDAD DE GRANADA, AVENIDA FUENTENUEVA S/N, 18002 GRANADA, SPAIN

ABSTRACT

We report the first attempt to date metasomatic events in peridotite xenoliths from the Subcontinental Lithospheric Mantle (SCLM) beneath the Cenozoic Calatrava volcanic field of central Spain. The most metasomatized xenoliths of the El Aprisco olivine melilitite maar were selected to perform a geochronological study on metasomatic apatite (U-Pb method) and amphibole (Ar-Ar), integrated with an enlarged chemical data set on these minerals. The metasomatic agents in studied samples are mainly carbonate-rich ultra-alkaline melts of probable asthenospheric derivation. Some samples have been overprinted by more than one metasomatic event. The geochronological data confirm three metasomatic events that occurred within the SCLM beneath central Spain in Cretaceous (118 Ma), Oligocene (29 Ma), and Miocene (16–4 Ma) times, much earlier than the host volcanic magmatism. To date, no magmatic events of those ages have been recorded in central Spain. However, a correlation with several cycles of sporadic intraplate magmatism of alkaline affinity in the Iberian microplate is suggested. This study illustrates that the SCLM preserves the memory of a complex history of melt and/or fluid percolation processes in a metasomatic record that is generally unrelated to shallower crustal magmatic events.

LITHOSPHERE; v. 11; no. 2; p. 192–208; GSA Data Repository Item 2019031 | Published online 27 December 2018 https://doi.org/10.1130/L1030.1

INTRODUCTION

Fluid or melt infiltration of the mantle in anorogenic settings may produce different styles of metasomatism, including modal, cryptic and stealth (e.g., Menzies et al., 1987; Ionov et al., 1997; O'Reilly and Griffin, 2013). The analyses of major, minor, and trace elements in metasomatic minerals (amphibole, clinopyroxene, apatite, phlogopite, carbonate) and interstitial glass, often associated with these minerals, is a powerful tool for unraveling the nature and composition of melts/fluids responsible for the different styles of metasomatism (e.g., Coltorti et al., 2007a; Raffone et al., 2009). Furthermore, several studies, based on the analysis of whole-rock or mineral separates, have attempted to date metasomatism of mantle rocks using an array of radiogenic isotopes (Rb-Sr, Sm-Nd, Pb-Pb, and Lu-Hf isochrons), but these have generally yielded spurious results (e.g., Nasir and Rollinson, 2009; Downes et al., 2015). Recently, the refinement of in situ analytical techniques for the Re-Os isotopic system has provided a more nuanced picture of the Re-Os system in base-metal sulfides and platinum-group elements from mantle-derived rocks, showing wide variability in the Os-isotope composition of these minerals (e.g., Alard et al., 2002; Ackerman et al., 2009). Such Os-isotope heterogeneity is reflected in complex distributions of Os-model ages recording the protracted passageway of melt/fluids through the mantle over a long period of time (e.g., González-Jiménez et al., 2013). Unfortunately, base-metal sulfides are highly sensitive to Re-Os isotopic isotopic exchange with Os-bearing fluid/melt(s), resulting in changes to the Re-Os isotopic system and mixed or meaningless model ages (Zangana, 1995). In this scenario, only when metasomatic minerals appear in amounts that are amenable to mineral separation or in situ techniques (zircon, apatite, amphibole, phlogopite) can dating success be achieved. Currently, the most widely used high-precision geochronometers are those employing the U-Pb method for accessory minerals and the $^{40}Ar/^{39}Ar$ method for K-rich minerals (Schmitz and Kuiper, 2013). The U-Pb method has been used in those rare mantle rocks that contain zircon (e.g., Zheng et al., 2006) or apatite (e.g., Morishita et al., 2008). The Ar-Ar dating method has been performed in the most common modal metasomatic minerals in mantle xenoliths: phlogopite (e.g., Wartho and Kelley, 2003; Hopp et al., 2008) and amphibole (e.g., Wartho and Kelley, 2003) and relies critically on the assumption of closed system behavior in the mantle environment.

Many peridotite xenoliths within volcanic rocks preserve a record of multi-stage metasomatism testifying to the percolation of magmatic melts and fluids within the lithospheric mantle. The potential correlation between events of metasomatism and events of magmatism recorded in the overlying crust is still unclear, suggesting that a significant portion of the magmatic budget that crosscuts a lithospheric section never reaches shallow crustal levels or the Earth's surface. One robust way to decipher the complexity of magmatic plumbing systems is to analyze and date the

*Corresponding author: granito@ucm.es

volcanic rocks (including their crystal cargo) and the metasomatic phases in peridotite xenoliths hosted by the volcanic rocks. The Calatrava volcanic field is an intraplate alkaline zone that has volcanic vents carrying mantle xenoliths of the Subcontinental Lithospheric Mantle (SCLM), which have recently been characterized (e.g., Bianchini et al., 2010; Villaseca et al., 2010; Lierenfeld and Mattsson, 2015). The involvement of different metasomatic agents in some of these peridotite xenolith suites (e.g., El Aprisco suite: Villaseca et al., 2010; González-Jiménez et al., 2014) provides an opportunity to precisely assess the chemical and temporal evolution of mantle metasomatic events, efforts not undertaken in previous studies of this volcanic field. Thus, the aims of this study are twofold: (1) to characterize and date metasomatic events in the lithospheric mantle beneath central Spain, and (2) to correlate these metasomatic events with the magmatism recorded in the Iberian Peninsula and its western Atlantic margin. Correlations of magmatic processes occurring at mantle depths with those exposed at the Earth's surface are anticipated to fill the gaps in knowledge of igneous processes occurring in central Iberia during Mesozoic and Cenozoic times. In order to achieve this goal we selected the most strongly metasomatized xenoliths of the El Aprisco olivine melilitite maar to perform a geochronological study on metasomatic apatite (U-Pb method) and amphibole (Ar-Ar dating), with an enlarged trace element and isotopic chemical data set for these minerals.

GEOLOGICAL SETTING

The Calatrava Volcanic Field (CVF) is an anorogenic intracontinental zone formed in Neogene time within the circum-Mediterranean province. This volcanic field comprises more than 200 volcanic centers in an area of around 5500 km^2 (Ancochea, 1982; Fig. 1) located at the boundary of small Cenozoic sedimentary basins that are transgressive over the Variscan basement (Fig. 1). The distribution of volcanic vents broadly follows Variscan shear bands reactivated by the main compressional axes of the Betic collision (Cebriá et al., 2011). Their geodynamic setting is still controversial, with debate focused around three main models: (1) volcanism related to asthenospheric-mantle upwelling (hot-spot or diapiric instabilities) in a pre-rifting stage (Ancochea, 1982; López-Ruiz et al., 1993); (2) a megafault system affecting the western Mediterranean (López-Ruiz et al., 2002); (3) uplifting of the Variscan basement with lithospheric folding in the Calatrava region exploiting a reactivation of previous NW–SE-trending Variscan structures formed during the indentation of the Betic block onto their foreland (Cebriá et al., 2011; Granja et al., 2015). Despite significant thickening during the Variscan orogeny, the Calatrava area has a normal crust (around 32 km) but a thin lithosphere (around 85 km; Granja et al., 2015).

Volcanism in Calatrava took place in two different stages (Ancochea, 1982): (1) a minor ultrapotassic event around 8.7–6.4 Ma ago and (2) alkaline basalts, basanites, and olivine nephelinites and melilitites from 3.7 to 0.7 Ma. The marked isotopic (Sr-Nd-Pb) homogeneity of the primary magmas of the main volcanic event suggests that the Calatrava volcanic rocks are derived from partial melting of an enriched homogeneous asthenospheric source (Ancochea 1982; Cebriá and López-Ruiz, 1995). The isotopic data suggest a HIMU-FOZO–like reservoir (where HIMU is high μ [μ = ^{238}U/^{204}Pb], and FOZO is a focal zone that has an approximate isotopic composition of ^{87}Sr/^{86}Sr = 0.7025, ε_{Nd} = +9, and ^{206}Pb/^{204}Pb = 19.5), similar to that defined for the European asthenospheric mantle (Wilson and Downes, 1991; Granet et al., 1995). An enriched asthenospheric reservoir is in agreement with the suggested presence of garnet and phlogopite within mantle sources based on the trace-element geochemistry of Calatrava volcanic rocks (e.g., Ancochea, 1982; López-Ruiz et al., 2002). A complex carbonatite-silicate association has recently been suggested from volcanic deposits in Calatrava (Bailey et al., 2005; Humphreys et al., 2010; Stoppa et al., 2012), but this is an open debate because some of the supposed mantle carbonates show isotopic evidence of sedimentary origins (Lustrino et al., 2016).

SAMPLES AND MINERALOGICAL FEATURES

Mantle xenoliths from the El Aprisco center (Universal Transverse Mercator Zone 30 S, 428483m E, 4299135m N), an olivine melilitite maar (Fig. 1), vary from lherzolite to wehrlite comprising four chemical groups on the basis of the degree and nature of the metasomatic agents (González-Jiménez et al., 2014). Group 1 and lherzolite 111658 of Group 2 are highly metasomatized peridotites affected by a carbonate-rich agent, whereas other peridotites show interaction with silica-undersaturated alkaline or subduction-related silicate melt/fluids (Groups 2, 3, and 4 of González-Jiménez et al., 2014). Lherzolites with the lowest incompatible trace element contents and having flat rare earth element (REE) patterns (Group 4) seem to be a slightly restitic peridotite source that is poorly metasomatized (González-Jiménez et al., 2014). The three xenoliths selected in this study for geochronological purposes are from Group 1 (two wehrlites: 111657 and the apatite-bearing 111659), and from Group 2 (lherzolite 111658 with accessory apatite).

Apatite only appears in two xenoliths: the 111659 wehrlite of the most metasomatized Group 1, and in the 111658 lherzolite of Group 2. It is always an accessory phase (< 0.3 modal %), being markedly rare in the Group 2 lherzolite, where it occurs as dispersed small grains (mostly < 100 μm) within mafic peridotite minerals that are in apparent microstructural equilibrium with the lherzolite mineral assemblage (Fig. 2D). In the wehrlite, apatite appears interstitially forming clustered polygonal dusty grains up to 1800 μm in diameter (Fig. 2A and 2B). Apatite is unrelated to the metasomatic amphibole but locally coincides with the network of interconnected intergranular veins of zeolitized glass (with accessory calcite) that penetrate the wehrlite 111659 (Fig. 2B). Nevertheless, textural and compositional studies indicate that apatite did not contribute to the formation of interstitial glass in these xenoliths (González-Jiménez et al., 2014).

Amphibole in selected samples appears as a main mineral phase (> 5 modal%), with a medium to coarse grain size (González-Jiménez et al., 2014). It forms veins or small layers in these peridotites. Only in lherzolite from Group 2 does the amphibole shows a clear corroded aspect and spatial relation with interstitial glass veins and pockets (González-Jiménez et al., 2014). Glass in these xenoliths may have been formed by in situ melting reactions promoted by amphibole breakdown during volcanic entrainment (Villaseca et al., 2010) or, alternatively, by infiltrating mantle metasomatic melts reacting with previous amphibole shortly before the entrainment of the xenoliths in the host basalt (González-Jiménez et al., 2014). The interconnected network of altered glass (zeolitized) with occasional calcite that appears in Group 1 xenoliths is clearly another metasomatic stage unrelated to apatite or amphibole formation/breakdown.

ANALYTICAL TECHNIQUES

In Situ Major and Trace Element Mineral Chemistry

New data on 50 major (electron microprobe) and 36 trace element (LA-ICP-MS) spot analyses have been added to the chemical data set of González-Jiménez et al. (2014) to yield a comprehensive body of geochemical information. Major-element compositions of silicates and apatite were analyzed in polished thick sections using a Jeol JXA-8900 M electron microprobe with four wavelength dispersive spectrometers at

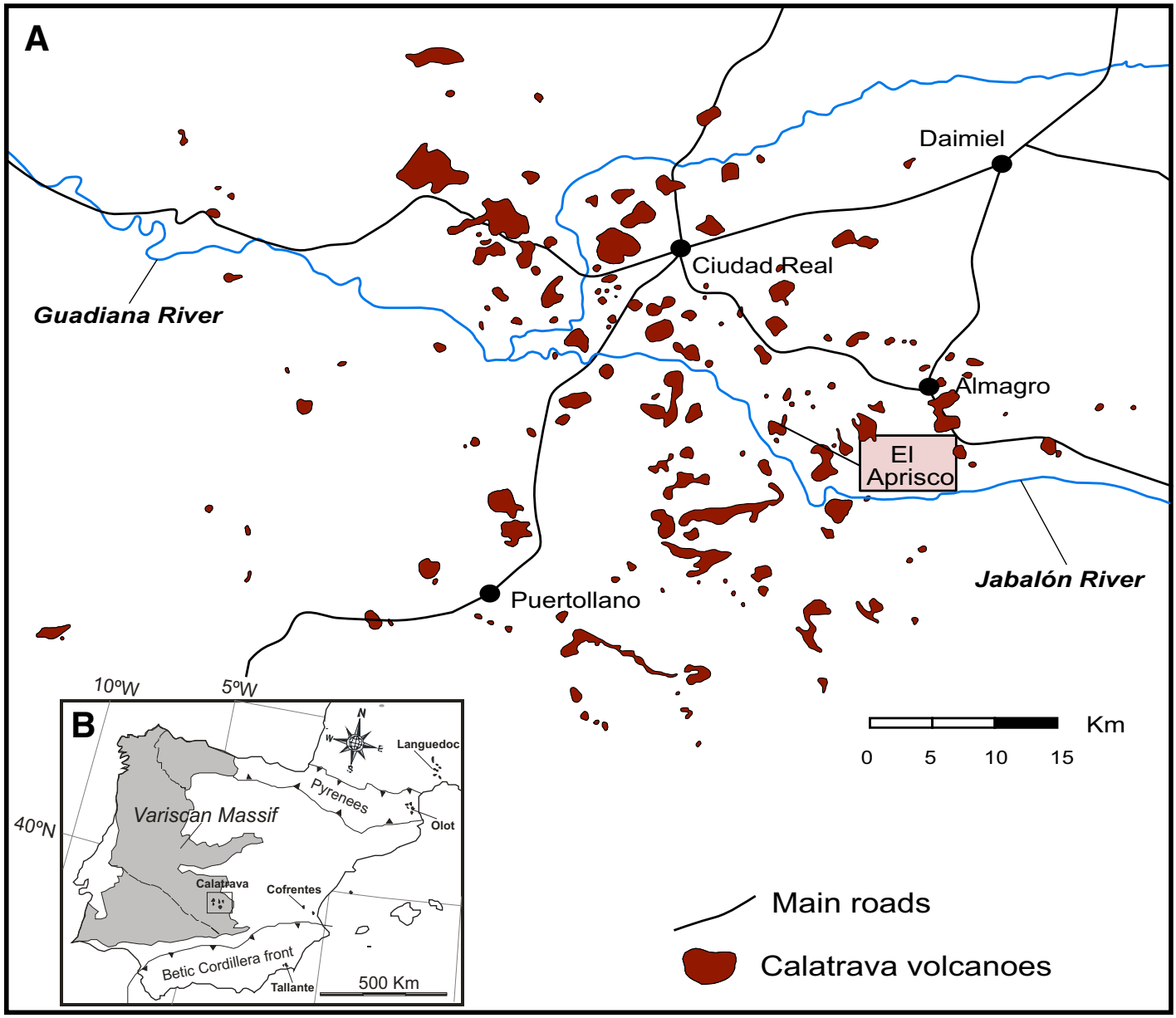

Figure 1. (A) Sketch map of the Calatrava Volcanic Field showing the location of the El Aprisco olivine melilitite maar, simplified after Ancochea (1982). (B) Inset of the Iberian Peninsula showing the location of the Cenozoic volcanic fields.

the Centro de Microscopía Electrónica "Luis Bru" (Universidad Complutense de Madrid, Spain). Analytical conditions included an accelerating voltage of 15 kV and an electron beam current of 20 nA, with a beam diameter of 5 µm. Elements were counted for 10 s on the peak and 5 s on each background position. Corrections were made using an online ZAF method. Detection limits are 0.02 wt% for Al, Na, K, and P; 0.03 wt% for Ti, Fe, Mn, Mg, Ni, and Cr; and 0.04 wt% for Si. The CO_2 contents of apatite were analyzed after Cr coating of polished samples and standards, and using an LDE2 crystal with counting times of 20 s on peak. Smithsonian dolomite (NMNH 10057) was used as the standard. On the basis of counting statistics, the carbon detection limit was less than 1200 ppm. We have checked this method by analyzing Durango apatite and, as expected, found no detectable carbon in it. We are therefore confident that our approach yields true carbon concentrations.

Trace elements (including REE, Ba, Rb, Sr, Ga, Th, U, Nb, Ta, Pb, Zr, Hf, Y, Sc, V, Co, and Ni) were determined in situ on clinopyroxene, amphibole, and apatite in polished thick sections, by laser ablation (LA-ICP-MS). This was done at the Geochemical Analysis Unit, Australian Research Council (ARC) Centre of Excellence for Core to Crust Fluid Systems (CCFS)/ARC National Key Centre for Geochemical Evolution and Metallogeny of Continents (GEMOC), using an Agilent 7500CS ICP-MS coupled to a New Wave UP 213 laser source. The counting time for one analysis was typically 180 s (60 s on gas blank to establish background and 120 s for signal collection). The diameter of the laser beam was around 40 µm, the frequency 5 Hz, and laser energy 8 J/cm^2. Ablation was performed in a He carrier gas (0.9–1.2 l/min). After exiting the sample cell, He was combined with Ar (0.9–1.2 l/min) gas in a 30 cm^3 mixing chamber prior to entering the ICP as described by Jackson et al. (2004).

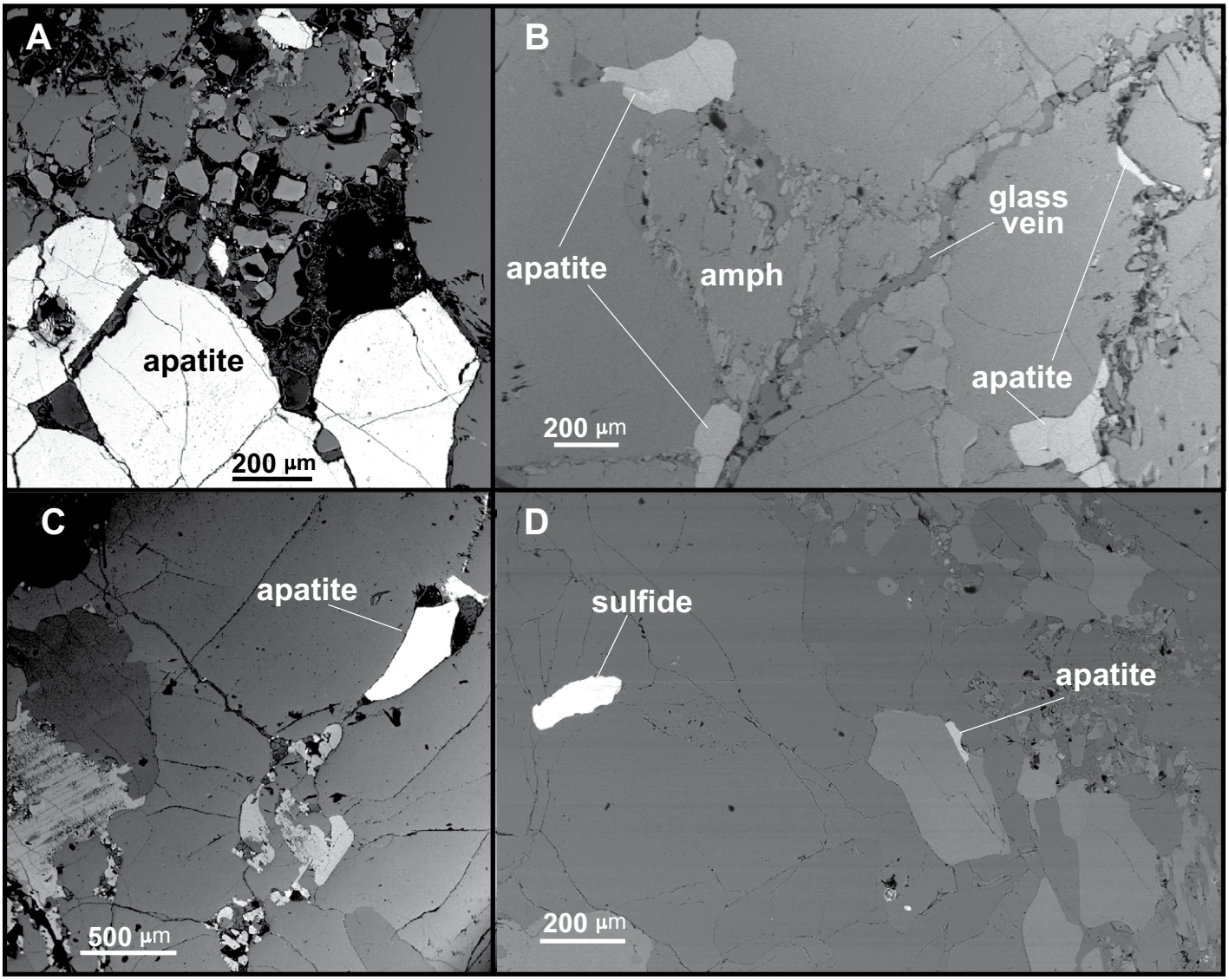

Figure 2. Backscattered electron images of apatite-bearing peridotite xenoliths from El Aprisco maar. (A) Cluster of big apatite crystals in wehrlite 111659. (B) Apatite crystals in wehrlite 111659 located near intergranular films of zeolitized glass (sometimes with accessory calcite). (C) Isolated big crystal of apatite (scale bar of 500 µm) in lherzolite 111658. (D) Interstitial apatite grain in lherzolite 111658.

The data were processed using the GLITTER software (Griffin et al., 2008). The NIST 610 glass standard was used to calibrate relative element sensitivities for the analyses of the silicate minerals. Each analysis was normalized to Ca using concentrations determined by electron microprobe. Detection limits for each element are in the range of 0.01–0.06 ppm except for Sc (0.11 ppm). Precision and accuracy (both better than 10%) were assessed from repeated analyses of the BCR-2 standard. Representative mineral chemical data are presented in Table 1.

Amphibole Ar-Ar Dating

Amphibole was concentrated by mineral separation methods. Five samples were selected for Ar-Ar dating, two metasomatic amphiboles from peridotite xenoliths, and three megacrysts (amphibole and phlogopite are ~6 and 4.5 cm in length, respectively) from host volcanic rocks. The small size of the 111659 wehrlite xenolith precluded separation of a sufficient quantity of amphibole from this sample. In contrast, the two amphibole megacrysts from Calatrava volcanic rocks were split in two subsets (Table 2). Samples were crushed, sieved to select the 400–500 µm fractions, and washed in deionized water. High purity grains were handpicked under a binocular microscope and ultrasonically cleaned using ethanol. Samples were placed in copper or aluminum foil packets, together with neutron flux monitors, and stacked in quartz tubes. The relative positions of packets were precisely measured (±0.5mm) for later reconstruction of neutron flux gradients. The sample package was irradiated in the Oregon State University reactor, Cd-shielded facility. Fish Canyon sanidine (28.294 ± 0.036 [1σ] Ma, Renne et al., 2011) was used to monitor ^{39}Ar production and establish neutron flux values (J) for the samples. The neutron flux within a given disc is calculated by least-squares fitting of a surface to the J-monitors. Estimated errors in the neutron flux measurements are calculated from the residual deviation from the fitted surface. Gas was extracted from samples via step-heating using a mid-infrared CO_2

TABLE 1. MAJOR-ELEMENT (WT%) AND TRACE-ELEMENT CONCENTRATIONS (IN PPM) FOR REPRESENTATIVE MINERALS OF PERIDOTITE XENOLITHS OF EL APRISCO MAAR

	Apatite							Clinopyroxene														Amphibole									
	111659					111658		111658					111657					72689						111657					72689				
	1	3	5	6	7			4	1	3	5	7	30	32	28	29	12	43	44	36	40	41	26	21	27	18	11	46	45	37	38	42
	wehrlite					lherzolite		lherzolite					wehrlite					lherzolite						wehrlite					lherzolite				
SiO_2	–	–	–	–	–	–	–	52.22	52.21	51.94	52.12	52.33	53.27	53.33	53.66	52.64	53.08	50.99	51.35	50.87	50.82	51.03	44.50	44.24	44.44	43.43	43.89	42.63	43.18	43.33	42.45	42.85
Al_2O_3	0.02	0.02	0.03	0.04	–	0.04	0.20	4.00	4.15	4.08	4.20	4.18	3.77	4.07	4.42	4.41	4.40	5.96	5.48	5.35	6.20	5.16	12.86	12.71	12.86	13.79	13.21	15.59	15.28	15.19	15.19	15.50
FeO	0.37	0.40	0.45	0.41	0.36	0.33	0.38	2.67	2.64	2.67	2.86	2.83	3.22	3.37	3.07	3.42	3.26	2.86	2.72	2.77	2.74	2.54	4.03	4.02	3.95	4.10	3.99	4.25	4.14	4.18	4.08	3.94
MnO	0.09	0.11	0.06	0.06	0.09	0.07	0.07	0.07	0.07	0.03	0.09	0.08	0.17	0.15	0.13	0.16	0.13	0.07	0.08	0.08	0.08	0.08	0.04	0.07	0.17	0.05	0.08	0.05	0.02	0.08	0.02	0.08
MgO	1.15	1.07	1.12	1.07	1.03	0.92	0.94	17.74	17.82	17.66	17.78	17.53	16.33	16.03	15.96	16.04	16.89	15.33	15.47	15.50	15.21	15.78	18.02	19.68	18.40	19.10	19.47	17.68	17.99	17.26	17.86	17.74
CaO	52.14	50.68	51.80	52.25	51.98	51.47	50.99	21.29	21.60	21.37	21.36	21.79	19.99	20.08	20.02	18.98	19.60	22.80	22.88	22.97	22.80	22.44	10.33	9.92	10.27	10.07	10.21	11.76	11.65	11.39	11.85	11.30
Na_2O	0.74	0.76	0.71	0.69	0.69	0.64	0.68	1.06	1.02	1.02	0.99	1.19	1.73	1.74	1.86	2.05	1.83	0.95	0.99	0.85	0.93	0.89	3.81	3.54	3.74	3.39	3.44	3.60	3.72	3.50	3.59	3.53
K_2O	0.01	–	0.01	–	0.01	0.02	0.02	0.02	0.00	0.01	–	–	0.01	–	0.00	–	0.00	–	–	–	0.01	–	1.02	0.99	1.06	1.00	1.22	0.03	0.03	0.02	0.02	0.00
TiO_2	–	–	–	–	0.03	0.01	–	0.09	0.08	0.10	0.13	0.10	0.06	0.12	0.08	0.14	0.12	0.41	0.39	0.36	0.42	0.31	0.77	0.74	0.80	0.72	0.90	1.04	1.09	0.85	0.83	0.86
P_2O_5	40.65	41.32	40.97	40.41	40.84	40.39	39.97	0.02	0.03	–	0.03	0.02	0.05	0.06	0.02	0.03	0.04	0.02	0.05	–	0.01	–	0.03	0.03	0.06	0.11	0.01	0.04	–	0.03	0.08	0.05
F	0.78	0.84	0.73	0.70	0.77	0.38	0.27	–	–	–	–	–	0.08	0.01	0.03	0.06	–	0.04	–	–	0.06	–	0.12	0.13	0.02	0.17	0.12	–	–	0.03	–	–
Cl	1.22	1.41	1.15	1.18	1.11	3.36	3.54	–	–	–	–	–	–	–	0.01	–	0.01	–	–	–	0.02	–	0.03	0.04	0.04	0.02	0.03	0.14	0.14	0.06	0.05	0.05
CO_2	1.32	1.05	2.01	1.52	0.84	0.80	1.59	nd	nd	nd	nd	nd	nd	nd	nd	nd	nd	nd	nd	nd	nd	nd	nd	nd	nd	nd	nd	nd	nd	nd	nd	nd
Cr_2O_3	–	0.02	–	–	0.01	0.02	–	0.67	0.66	0.67	0.62	0.68	0.81	0.97	0.93	1.13	0.87	0.68	0.59	0.66	0.57	0.52	1.76	1.66	1.62	2.12	1.22	0.80	0.75	0.80	0.85	0.91
Total	97.75	96.89	98.32	97.63	97.09	98.45	98.65	99.90	100.39	99.66	100.25	100.72	99.57	99.97	100.22	99.02	100.23	100.15	100.00	99.42	99.88	98.81	97.27	97.79	97.50	98.03	97.87	97.65	98.05	96.70	96.97	96.83
Sc	0.46	0.37	1.17	0.74	0.53	13.45	2.70	65.4	63.4	66.3	63.8	61.9	45.6	46.7	48.7	46.5	48.5	66.1	66.5	67.3	68.2	60	38.6	33.1	38.8	34.3	34.1	59.2	58.7	52.9	50.5	52.6
V	7.58	7.86	7.58	7.77	7.37	56.52	26.13	262	233	280	242	236	180	197	196	189	187	319	314	323	298	286	349	290	331	294	289	438	461	392.8	317	358
Co	1.48	1.48	4.80	4.10	1.41	13.31	88.3	38.8	29	36.5	31.8	30	27.14	26.89	27.6	24.9	27.2	27.7	29.8	33.6	24.7	34.1	53.4	46.3	54.5	47.7	46.7	50.3	61.5	45.2	35.8	44.9
Ni	4.46	4.32	52	7.40	4.34	273	1572	671	438	654	715	528	439	419	426	409	438	440	466	499	377	485	1181	1037	1228	1057	1024	1088	1765	996	810	1115
Ga	12.56	15.17	16.20	14.97	30.84	13.63	12.06	21.39	11.9	23	12.66	14.41	7.41	7.87	8.14	7.6	7.15	4.75	4.61	5.19	3.58	5.59	26.6	23.95	29.3	22.4	23.6	29.92	34.9	24.78	13.3	22.9
Rb	0.04	0.05	0.95	0.02	0.02	23.84	16.88	1.98	0.92	2.37	2.47	1.4	–	–	0.35	–	–	–	–	–	–	–	21.7	15.1	19	18.13	17.2	0.85	1.7	1.46	0.73	1.54
Sr	7250	6690	6710	6890	6730	8395	10275	628	539	679	505	502	307	300	329	277	309	97.6	101	102	78.9	93.2	569	455	523	460	473	318	313	337	272	306
Y	182	174	176	183	181	77.56	104	16.48	14.71	18	15.41	14.86	20.07	21.17	23.5	21.17	22.15	17.12	15.25	15.28	17.13	15.45	22	19.59	22.5	20.3	20.41	22.5	21.32	20.26	17.6	20.08
Zr	15.29	19.71	21.71	19.28	16.23	1.96	0.94	9.2	7.96	9.15	8.02	7.86	169	186	195	189	182.4	10.77	9.51	9.94	10.47	9.4	271	213	256	256	256	9.22	9.47	8.54	7.87	8.67
Nb	0.74	0.79	2.95	0.69	0.67	1.50	1.25	9.58	4.88	11.6	4.9	5.36	1.84	1.93	3.47	2.08	1.32	–	0.02	–	–	–	206	157	184	188	185	0.15	0.36	0.03	0.04	0.05
Ba	124	123	164	123	122	626	535	320	146	344	159	191	0.63	0.74	10.2	0.43	0.09	0.07	0.06	0.22	0.39	5.20	195	178	226	141	166	601	640	490	199	385
La	1114	1077	1112	1116	1117	3104	3802	48.5	42.2	62.2	43.9	45	10.94	11.07	16.6	11.27	11.18	14.99	14.58	18.24	16.87	16.74	15.2	12.4	14.21	13.61	13.44	21.9	20.26	24.48	21.4	23.33
Ce	2240	2132	2205	2199	2226	4713	4926	110	98.8	122	102	103	42.5	43.3	52.4	43.6	43.3	18.09	18.68	25	20.33	21.75	59.1	46.5	51.4	50.1	51.8	28.85	29.37	34.69	28.4	31.9
Pr	222	216	229	226	225	311	361	12.35	11.15	14.67	11.35	11.6	6.74	6.81	8.45	7.03	6.85	1.16	1.27	1.65	1.22	1.42	8.83	7.11	7.73	7.59	7.45	2.04	2.12	2.44	2.08	2.37
Nd	800	764	787	787	793	729	846	42.9	39.7	51	39.6	39.5	32.4	33.8	40.1	34.5	33.4	3.63	3.8	4.82	3.86	4.21	42.2	34.7	36.9	36.9	35.5	6.23	6.29	7.14	6.47	7.24
Sm	115	111	114	116	116	54.25	60.83	5.95	5.63	6.59	5.37	5.32	7.57	7.77	8.99	8.31	7.95	1.33	1.18	1.27	1.28	1.25	9.19	8.11	8.76	8.58	8.15	1.71	1.63	1.78	1.51	1.618
Eu	29.67	28.72	30.20	30.30	30.57	13.16	13.9	1.65	1.52	1.85	1.58	1.51	2.27	2.38	2.81	2.59	2.51	0.58	0.51	0.54	0.55	0.51	2.85	2.49	2.74	2.66	2.63	0.75	0.72	0.69	0.58	0.63
Gd	88.70	87.60	90.60	92.80	92.50	28.58	34.04	4.06	3.81	4.54	3.9	3.73	5.98	6.11	7.38	6.78	6.59	2.01	1.81	1.95	2.17	1.94	7.04	6.23	6.97	6.94	6.55	2.53	2.55	2.5	2.15	2.4
Tb	9.23	8.91	9.15	9.39	9.53	3.1	2.98	0.57	0.48	0.60	0.50	0.49	0.81	0.83	1.01	0.91	0.89	0.40	0.34	0.36	0.39	0.37	0.93	0.83	0.97	0.93	0.86	0.50	0.47	0.46	0.39	0.45
Dy	43.90	42.10	43.00	44.10	44.90	16.05	16.56	3.24	2.95	3.50	2.96	2.88	4.66	4.70	5.77	5.26	5.04	2.99	2.64	2.74	3.02	2.69	5.19	4.57	5.20	5.04	4.70	3.81	3.56	3.50	2.79	3.33
Ho	7.10	6.87	7.08	7.32	7.20	2.61	3.28	0.62	0.57	0.68	0.57	0.57	0.83	0.87	1.01	0.92	0.89	0.67	0.60	0.60	0.65	0.60	0.92	0.83	0.95	0.89	0.84	0.84	0.79	0.77	0.62	0.74
Er	16.59	16.36	16.71	17.17	16.69	6.71	7.47	1.70	1.61	1.93	1.59	1.56	2.05	2.12	2.51	2.22	2.20	1.94	1.77	1.78	2.01	1.83	2.19	2.00	2.20	2.16	2.00	2.58	2.42	2.31	1.99	2.28
Tm	1.86	1.80	1.83	1.88	1.87	0.81	0.88	0.25	0.21	0.25	0.22	0.22	0.26	0.27	0.32	0.31	0.29	0.29	0.25	0.25	0.29	0.26	0.28	0.24	0.28	0.28	0.27	0.39	0.35	0.36	0.29	0.34
Yb	9.86	9.40	9.91	10.06	10.13	5.04	5.9	1.76	1.55	1.88	1.54	1.49	1.65	1.76	1.90	1.73	1.67	1.90	1.69	1.96	2.13	1.91	1.74	1.48	1.58	1.56	1.41	2.76	2.80	2.60	2.10	2.49
Lu	1.29	1.25	1.27	1.33	1.31	0.76	0.79	0.23	0.20	0.23	0.22	0.20	0.20	0.21	0.26	0.26	0.24	0.27	0.23	0.23	0.25	0.24	0.21	0.18	0.21	0.20	0.21	0.36	0.32	0.33	0.30	0.31
Hf	0.02	0.09	0.15	0.09	0.09	0.12	0.03	0.41	0.43	0.35	0.37	0.33	2.33	3.01	3.35	3.36	2.85	0.67	0.60	0.63	0.59	0.56	3.97	2.68	3.05	4.00	4.40	0.43	0.54	0.44	0.44	0.46
Ta	0.00	0.03	0.25	0.02	0.02	0.02	0.02	0.06	0.03	0.09	0.03	0.02	0.18	0.23	0.30	0.28	0.21	–	–	–	–	–	10.70	6.02	6.91	10.18	10.31	–	–	–	–	–
Pb	12.15	11.65	11.92	12.03	12.10	21.14	30.23	3.05	2.38	3.37	2.57	2.58	0.27	0.26	0.34	0.27	0.22	1.45	1.42	1.43	1.33	1.31	0.63	0.62	0.66	0.62	0.57	5.65	6.04	4.50	3.40	4.26
Th	148	139	145	141	139	730	923	7.95	6.68	7.67	7.09	7.15	0.31	0.36	0.85	0.41	0.34	2.90	2.53	4.58	4.75	4.39	0.42	0.35	0.46	0.43	0.39	3.28	3.12	4.72	3.81	4.70
U	40.90	38.40	40.40	38.78	38.40	190	223	1.91	1.75	2.06	1.82	1.84	0.07	0.08	0.23	0.09	0.08	1.24	1.15	1.81	1.68	1.57	0.12	0.11	0.10	0.11	0.13	1.33	1.30	1.66	1.36	1.42

Note: nd—not determined.

TABLE 2. Ar-Ar DATA FROM AMPHIBOLE AND PHLOGOPITE FROM CALATRAVA VOLCANIC ROCKS AND PERIDOTITE XENOLITHS

Sample	Rock type	Mineral		Volcano	Plateau age						Inverse Isochron							Youngest population (max. age)				
					%^{39}Ar	Age (Ma)	±2σ	MSWD	P	n	Age (Ma)	±2σ	^{40}Ar/^{36}Ar(i)	±2σ	MSWD	P	n	Age (Ma)	±2σ	MSWD	P	n
111657	wehrlite	amph	metasomatic	El Aprisco	–	–	–	–	–	–	*15.3*	*1.5*	*320*	*100*	–	–	*2*	**15.7**	0.3	0.2	0.65	2
111658	lherzolite	amph	metasomatic	El Aprisco	–	–	–	–	–	–	*4.3*	*1.2*	*297*	*4*	–	–	*3*	**3.9**	0.7	1.4	0.26	3
114404a	basalt	amph	megacryst	El Aprisco	–	–	–	–	–	–	*2.7*	*0.4*	*292*	*15*	–	–	*4*	2.6	0.2	0.2	0.88	4
114404b	basalt	amph	megacryst	El Aprisco	–	–	–	–	–	–	*2.7*	*0.2*	*308*	*11*	–	–	*4*	**2.8**	0.1	1.6	0.2	4
111653a	basalt	amph	megacryst	C. Pelado	60	1.59	0.07	0.25	0.97	8	1.57	0.24	299.4	9.2	0.28	0.95	8	–	–	–	–	–
111653b	basalt	amph	megacryst	C. Pelado	66	1.8	0.06	1.5	0.17	7	1.95	0.17	293.8	5.3	1.1	0.36	7	–	–	–	–	–
114403	basalt	phlog	megacryst	C. Pelado	53	**2.23**	0.04	1.12	0.34	4	2.11	0.15	303	5.2	0.23	0.79	4	–	–	–	–	–

Note: Preferred ages are marked in bold. Values in italics (inverse isochron) are based in the youngest population. ^{40}Ar/^{36}Ar(i)—non-radiogenic intercept value; P—probability that the residuals can be explained by measurement errors alone; n—number of accepted steps (out of the total number of steps run).

laser, with samples housed in a doubly pumped ZnS-window laser cell. Individual sample grains were loaded into a copper planchette containing 1x1 cm square wells. Liberated argon was then purified of active gases (e.g., CO_2, H_2O, H_2, N_2, CH_4) using three Zr-Al getters, one at 16 °C and two at 400 °C. Data were collected on a GVi instrument ARGUS 5-collector mass spectrometer using a variable sensitivity faraday collector array in static collection (non-peak hopping) mode (Sparks et al., 2008; Mark et al., 2009), at the NERC Argon Isotope Facility of the SUERC. Time-intensity data are regressed to t_0 with second-order polynomial fits to the data. Mass discrimination was monitored by comparison to running-average values of an air standard. The average total system blank for laser extractions, measured between each sample run, was 1×10^{-15} mol for ^{40}Ar, 3×10^{-17} mol for ^{39}Ar, 3×10^{-18} mol for ^{36}Ar. All data are blank, with interference and mass discrimination corrected using the Masspec software package (authored by Al Deino, Berkeley Geochronology Center).

Plateau criteria included the following: the plateau consists of at least three contiguous steps, and the scatter between the ages of the steps is low, i.e., mean square of weighted deviates (MSWD) close to 1, and the fraction of ^{39}Ar released for these steps is ≥50%. Isochrons are calculated using only the plateau steps to confirm the composition of the trapped component. Generally, a plateau age is accepted if it is concordant at the 2σ level with the isochron age, has a trapped component indistinguishable from air (298.56 ± 0.31, 1σ) at the 2σ level, and meets the other criteria listed above. However, we note that the data for metasomatic amphiboles appear to be a mixture between excess and radiogenic Ar. Therefore, uncertainties on the trapped component compositions derived from the inverse isochron regressions are large and highly sensitive to individual data points. It is for this reason that we assume atmospheric trapped components in the amphiboles for purposes of plateau calculation. Summary data are presented in Table 2.

In Situ Apatite U-Pb Dating

U-Pb dating of apatite is difficult due to its generally low U contents and incorporation of common lead during formation (e.g., Thomson et al., 2012). In addition, LA-ICP-MS U-Pb dating of apatite also presents laser-induced U-Th-Pb fractionation and yields high age uncertainties in young Cenozoic crystals (Chew et al., 2011). Nevertheless, the new well-characterized matrix-matched reference apatites and the usually high U contents of metasomatic mantle apatite combine to make in situ apatite U-Pb dating a promising chronometer of metasomatic events in peridotite xenoliths. Indeed, studied metasomatic apatite has > 38 ppm U (Table 1), making it suitable for U-Pb dating.

Thick (85 µm) polished sections were mounted close to a 2.5-cm diameter epoxy disk containing four apatite reference material (Kovdor, Slyudyanka, Mount McClure, and Emerald Lake) and two zircon standards (GJ and 91500) to control instrument stability. Analyses were performed in situ using a 213 nm Nd:YAG laser microprobe attached to an Agilent 7500 quadrupole ICP-MS system at the GEMOC laboratories. Samples were ablated using a 55 µm (40 µm in the small apatite from sample 111658) laser beam that was rastered over the sample surface to create a 200 µm line to minimize laser-induced Pb/U fractionation. The laser energy was set at 6.5J/cm^2, with a 5Hz repetition rate. He carrier gas transports the ablated sample from the laser-ablation cell via a mixing chamber to the ICP-MS torch with the same gas flow conditions (0.9–1.2 L/min) as used for the ICPMS trace-element work.

Slyudyanka carbonatite apatite was used as a calibration standard due to its chemical homogeneity. Together with every six analyses of unknowns, well-characterized zircons (91500 and Mud Tank), and apatites have been analyzed as a quality control to monitor variability in operation conditions. The list of "check up" apatites includes Kovdor carbonatite (377.5 ± 3.5 Ma, Amelin and Zaitsev, 2002), Mt McClure syenite (523.5 ± 1.5 Ma, Schoene and Bowring, 2006), and Emerald Lake granite (92.2 ± 0.9 Ma, Coulson et al., 2002). Their analyzed weighted-mean ^{207}Pb-corrected ages agree within the published analytical results (367 ± 13, 538 ± 8 Ma, 99 ± 9 Ma, respectively) (GSA Data Repository Figure DR1[1]), mostly falling within the uncertainty limits on the assumed ages of the reference material.

Isotopic ratios and uncertainties on individual analyses are presented with 2σ errors in Table 3. Tera-Wasserburg concordia and weighted average ages were calculated using Isoplot Ex 3.0 (Ludwig, 2003).

In Situ Apatite Sr-Nd Isotopic Ratios

Only large apatite crystals of wehrlite 111659 were amenable to in situ Sr-Nd isotopic analyses. Eleven analyses close to previous U-Pb spots were ablated during Sr and Nd isotopic measurements at the Geochemical Analysis Unit at CCFS/GEMOC with a Wave/Merchantek UP 213 laser microprobe with a modified ablation cell coupled with a Nu Plasma Multicollector ICP-MS. During the ablation runs, ion beams were collected using a mix of Faraday cups and ion counters. The laser was fired at a frequency of 5 Hz (90%–95% power and fluency of 5–10 J/cm^{-2}) and a spot size of 65–100 µm (40–55 µm for some apatite spots). During ablation runs, the Sr and Nd analyses were monitored by repeated measurements of the Ice River perovskite standard (with $^{87}Sr/^{86}Sr = 0.70293 \pm 2$ and $^{143}Nd/^{144}Nd = 0.512615 \pm 9$, Yang et al., 2009) and the Batbjerg clinopyroxene standard ($^{87}Sr/^{86}Sr = 0.70444 \pm 9$, Neumann, 2004). The IR perovskite analyses yielded $^{87}Sr/^{86}Sr = 0.70287 \pm 6$ (1SE) and $^{143}Nd/^{144}Nd = 0.512608 \pm 24$ (1SE), whereas the Batbjerg clinopyroxene gave $^{87}Sr/^{86}Sr = 0.70453 \pm 5$ (1 standard error [SE]), which are within the uncertainty of the accepted values.

Isotopic ratios and uncertainties on individual analyses are presented with 2σ errors in Table 4.

MINERAL CHEMISTRY

Most of the trace-element signatures of wehrlites from Group 1 of El Aprisco, such as their convex upward LREE enriched REE patterns combined with prominent positive Nb-Ta and small negative Hf and Ti anomalies (fig. 4 of González-Jiménez et al., 2014), are inherited from the trace element composition of the abundant metasomatic amphibole (14–18 vol% in modal amount). Primary clinopyroxene in wehrlites does not present positive Nb-Ta anomalies in its multitrace element pattern and has lower LILE-Ti contents than associated amphibole (Table 1). Nevertheless, they share a similar REE pattern and small negative Pb-Sr-Hf-Ti anomalies in multi-trace element patterns suggesting an approach to chemical equilibrium shared between the two minerals, as departures from a $D^{amp/cpx}$ of 1 occur in elements (Nb, Ta, Ti, Ba), which usually show higher partition coefficients in peridotite amphibole (e.g., Chazot et al., 1996a; Raffone et al., 2009).

[1]GSA Data Repository Item 2019031, Figure DR1: Tera Wasserburg concordia diagrams (left column) and weighted average ^{207}Pb-corrected ages (right column) for the Kovdor, Mount McClure, and Emerald Lake apatite standards during LA-ICP-MS analyses; Figure DR2: $^{40}Ar/^{39}Ar$ incremental heating results and inverse isochrons plots for amphibole megacryst of the olivine melilitite 114404, and for metasomatic amphiboles of wehrlite 111657 and lherzolite 111658, all samples from the El Aprisco maar; and Figure DR3: $^{40}Ar/^{39}Ar$ incremental heating results and inverse isochrons plots for megacrystic 111653 amphibole and 114403 phlogopite of the olivine nephelinite from the Cerro Pelado scoria cone, is available at http://www.geosociety.org/datarepository/2019, or on request from editing@geosociety.org.

TABLE 3. ISOTOPIC AND AGE DATA FOR APATITE FROM PERIDOTITE XENOLITHS OF EL APRISCO MAAR

	$^{207}Pb/^{206}Pb$	2 SE	$^{207}Pb/^{235}U$	2 SE	$^{206}Pb/^{238}U$	2 SE	$^{208}Pb/^{232}Th$	2 SE	$^{207}Pb/^{206}Pb$ age (Ma)	2 SE	$^{207}Pb/^{235}U$ age (Ma)	2 SE	$^{206}Pb/^{238}U$ age (Ma)	2 SE	$^{208}Pb/^{232}Th$ age (Ma)	2 SE
Wehrlite 111659																
1	0.6450	0.0132	6.3085	0.1445	0.0735	0.0021	0.3148	0.0530	4612.7	30	2019.6	20	457.4	12	5532.3	814
2	0.6416	0.0134	6.1808	0.1426	0.0724	0.0020	0.3084	0.0517	4605.1	30	2001.7	20	450.7	12	5432.9	799
3	0.6424	0.0136	6.1759	0.1435	0.0723	0.0020	0.3107	0.0519	4606.9	30	2001.1	20	449.8	12	5469.2	800
4	0.6404	0.0145	6.3543	0.1542	0.0746	0.0022	0.3177	0.0525	4602.6	33	2026.0	21	463.7	13	5577.0	805
5	0.6482	0.0140	6.2913	0.1477	0.0730	0.0021	0.3142	0.0521	4619.9	31	2017.2	21	454.0	12	5523.0	802
6	0.6447	0.0146	5.7327	0.1389	0.0668	0.0019	0.2831	0.0461	4612.1	33	1936.3	21	417.1	12	5039.0	727
7	0.6569	0.0153	6.1059	0.1491	0.0699	0.0021	0.2903	0.0451	4639.3	33	1991.1	21	435.3	12	5151.5	707
8	0.6568	0.0144	6.1717	0.1454	0.0706	0.0020	0.3044	0.0490	4638.9	32	2000.5	21	440.0	12	5370.7	759
9	0.6626	0.0141	6.2853	0.1438	0.0713	0.0020	0.2990	0.0480	4651.7	30	2016.4	20	444.0	12	5286.9	748
10	0.6544	0.0157	6.1485	0.1520	0.0706	0.0021	0.2852	0.0438	4633.7	34	1997.2	22	439.9	13	5071.7	689
11	0.6532	0.0146	7.3572	0.1750	0.0847	0.0024	0.3635	0.0568	4631.1	32	2155.8	21	523.9	14	6266.7	842
12	0.6577	0.0141	6.7925	0.1572	0.0776	0.0022	0.3320	0.0528	4641.0	31	2084.7	20	482.0	13	5794.4	801
13	0.6581	0.0142	6.7713	0.1594	0.0774	0.0022	0.3622	0.0630	4641.7	31	2082	21	480.4	13	6247.1	935
14	0.6560	0.0139	6.8197	0.1609	0.0782	0.0022	0.3588	0.0618	4637.3	30	2088.3	21	485.1	13	6197.3	919
15	0.6456	0.0132	6.6770	0.1542	0.0778	0.0022	0.3476	0.0570	4614.0	29	2069.6	20	482.7	13	6029.8	854
16	0.6466	0.0133	6.8380	0.1597	0.0795	0.0023	0.3691	0.0608	4616.3	29	2090.7	21	493.2	14	6350.0	898
17	0.6460	0.0145	6.6981	0.1658	0.0780	0.0023	0.3543	0.0609	4615.1	32	2072.4	22	483.9	14	6130.6	909
18	0.6593	0.0152	6.9238	0.1760	0.0790	0.0024	0.3513	0.0596	4644.5	33	2101.7	23	490.0	14	6085.6	892
19	0.6623	0.0144	7.1192	0.1750	0.0808	0.0024	0.3810	0.0644	4650.9	31	2126.4	22	501.1	14	6524.1	942
20	0.6513	0.0140	7.0385	0.1706	0.0812	0.0024	0.3649	0.0598	4626.9	31	2116.3	22	503.5	14	6288.0	886
21	0.6613	0.0174	7.2997	0.2046	0.0830	0.0027	0.3761	0.0635	4648.7	38	2148.8	25	514.0	16	6452.3	933
22	0.6626	0.0137	7.2608	0.1750	0.0824	0.0024	0.3794	0.0666	4651.7	30	2144.0	22	510.4	14	6500.8	976
23	*0.6840*	*0.0193*	*7.0282*	*0.2032*	*0.0772*	*0.0026*	*0.3589*	*0.0646*	*4697.6*	*40*	*2115.0*	*26*	*479.6*	*16*	*6199.2*	*960*
24	*0.6733*	*0.0140*	*7.2168*	*0.1759*	*0.0806*	*0.0024*	*0.3693*	*0.0651*	*4674.8*	*30*	*2138.6*	*22*	*499.7*	*14*	*6353.2*	*961*
25	*0.6769*	*0.0143*	*7.1358*	*0.1748*	*0.0793*	*0.0023*	*0.3667*	*0.0651*	*4682.3*	*30*	*2128.5*	*22*	*491.9*	*14*	*6314.4*	*963*
26	0.6695	0.0152	6.8516	0.1753	0.0770	0.0023	0.3502	0.0630	4666.7	33	2092.4	23	478.0	14	6068.7	943
27	0.6700	0.0148	7.1763	0.1793	0.0806	0.0024	0.3760	0.0680	4667.6	32	2133.6	22	499.6	14	6451.0	999
Lherzolite 111658																
1	0.6160	0.0164	4.9147	0.1297	0.0599	0.0019	0.2069	0.0343	4546.3	38	1804.8	22	374.9	11	3801.8	575
2	0.6377	0.0169	4.5213	0.1217	0.0532	0.0017	0.1709	0.0297	4596.4	38	1734.9	22	334.4	10	3188.3	513
3	0.6407	0.0156	4.8831	0.1245	0.0573	0.0017	0.1860	0.0325	4603.1	35	1799.3	22	359.1	11	3447.9	554
4	0.5964	0.0238	4.1306	0.1398	0.0521	0.0020	0.1719	0.0257	4499.2	57	1660.4	28	327.5	12	3206.6	444
5	0.6298	0.0166	4.7228	0.1271	0.0563	0.0018	0.1726	0.0293	4578.3	38	1771.3	23	353.4	11	3217.8	505
6	0.6370	0.0156	5.0058	0.1288	0.0591	0.0018	0.1809	0.0315	4594.6	35	1820.3	22	370.0	11	3360.0	538
7	0.5023	0.0280	2.6956	0.1210	0.0402	0.0019	0.1169	0.0150	4248.1	81	1327.3	33	254.2	12	2233.7	272
8	0.6008	0.0241	4.3075	0.1527	0.0539	0.0021	0.1834	0.0289	4509.9	58	1694.8	29	338.3	13	3404.2	493
9	0.5571	0.0331	3.7342	0.1971	0.0494	0.0020	0.0170	0.0005	4399.9	86	1578.7	42	311.0	13	340.1	9
10	0.5643	0.0561	3.5821	0.3057	0.0467	0.0028	0.0185	0.0007	4418.7	141	1545.6	68	294.5	17	369.9	14
11	0.5630	0.0398	3.8680	0.2423	0.0507	0.0024	0.0172	0.0005	4415.2	101	1607.0	51	319.1	14	344.0	10
12	*0.5856*	*0.0801*	*3.2603*	*0.3822*	*0.0411*	*0.0032*	*0.0173*	*0.0009*	*4472.6*	*192*	*1471.6*	*91*	*259.5*	*20*	*347.4*	*17*

Note: Data in italics represent highly discordant analyses. SE—standard error.

TABLE 4. ISOTOPIC (Sr, Nd) COMPOSITION OF APATITE FROM WEHRLITE 111659 OF EL APRISCO MAAR

Sample	$^{87}Rb/^{86}Sr$	1 SE	$^{87}Sr/^{86}Sr$	1 SE	$(^{87}Sr/^{86}Sr)_{30}$	$^{147}Sm/^{144}Nd$	1 SE	$^{143}Nd/^{144}Nd$	1 SE	$(^{143}Nd/^{144}Nd)_{30}$	$\varepsilon(Nd)_{30}$	1 SE	T_{DM}
111659-01	0.001178	0.000210	0.703370	0.000061	0.703369	0.081899	0.000170	0.513215	0.000094	0.513199	11.7	1.8	–0.07
111659-02	0.000309	0.000053	0.703277	0.000044	0.703277	0.081679	0.000190	0.513012	0.000160	0.512996	7.7	3.1	0.16
111659-03	0.009098	0.002900	0.703296	0.000085	0.703292	0.082959	0.000190	0.512933	0.000090	0.512917	6.2	1.8	0.25
111659-04	0.004171	0.000850	0.703273	0.000056	0.703271	0.081077	0.000210	0.512592	0.000110	0.512576	–0.5	2.1	0.64
111659-05	0.002242	0.000360	0.703320	0.000050	0.703319	0.084766	0.000300	0.513120	0.000088	0.513103	9.8	1.7	0.04
111659-06	0.000074	0.000016	0.703256	0.000061	0.703256	0.085370	0.000170	0.513214	0.000056	0.513197	11.7	1.1	–0.08
111659-07	0.000049	0.000015	0.703318	0.000055	0.703318	0.085910	0.000290	0.512581	0.000068	0.512564	–0.7	1.3	0.68
111659-08	0.000010	0.000014	0.703369	0.000058	0.703369	0.085674	0.000200	0.512715	0.000070	0.512698	1.9	1.4	0.52
111659-09	0.000017	0.000011	0.703331	0.000054	0.703331	0.083849	0.000200	0.512908	0.000080	0.512892	5.7	1.6	0.29
111659-10	0.001163	0.000230	0.703320	0.000055	0.703320	0.082552	0.000140	0.512907	0.000094	0.512891	5.7	1.8	0.28
111659-11	0.001358	0.000390	0.703243	0.000077	0.703242	0.080685	0.000190	0.512753	0.000089	0.512737	2.7	1.7	0.46

Note: Initial isotopic ratios calculated at 30 Ma. SE—standard error; T_{DM}—depleted mantle model age.

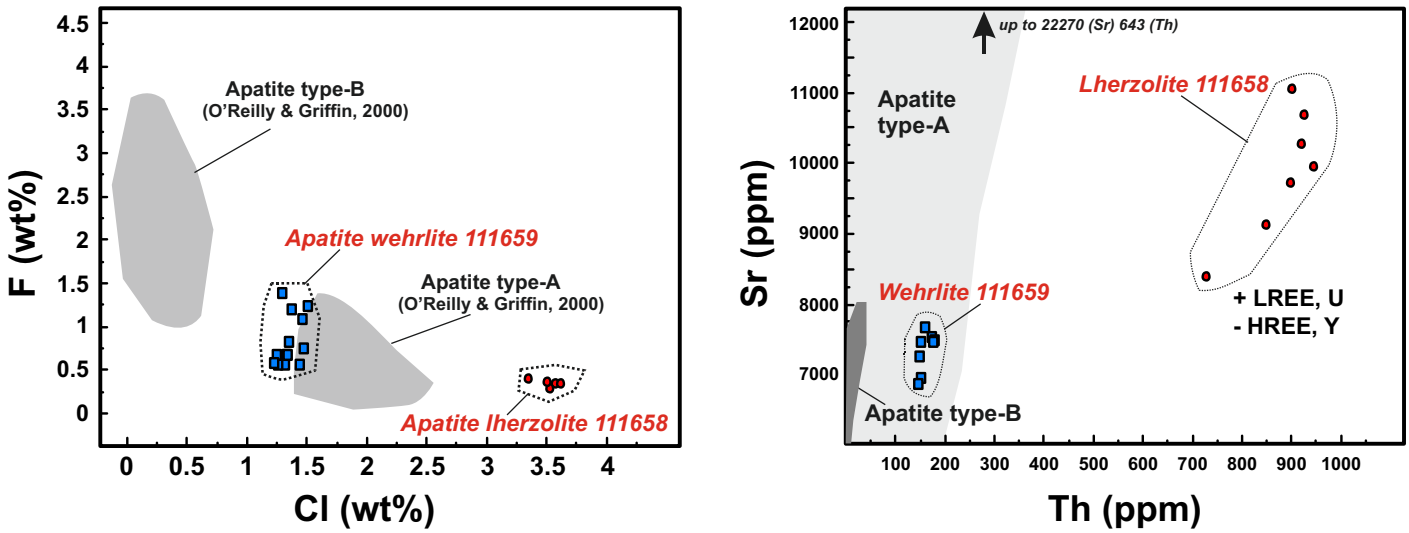

Figure 3. Chemical data of apatite in peridotite xenoliths from El Aprisco. REE—rare earth element (L—light, H—heavy).

As in wehrlites, the slightly high LILE, Nb, Ta, and Ti contents of the amphibole from lherzolite 111658 (Group 2) also indicate chemical equilibrium with respect to the composition of the associated clinopyroxene, and are evidence of the metasomatism undergone by the studied peridotite xenoliths (see also González-Jiménez et al., 2014).

Petrographical features of apatite in studied xenoliths are similar to the dispersed grains of apatite-A described by O'Reilly and Griffin (2000), i.e., dusty crystals not associated with modal amphibole. The relatively high MgO (up to 1.17 wt%), FeO (0.54 wt%) and Na_2O (0.80 wt%) contents are also in agreement with values found in apatite-A of mantle xenoliths. Moreover, apatite of El Aprisco xenoliths enlarges the compositional field of metasomatic A-type apatite in peridotites showing higher halogen, REE, and U contents (Fig. 3). The high Sr (6700–11050 ppm), Th (140–950 ppm), U (38–220 ppm), Ce (2400–5600 ppm), and low Y (80–200 ppm) contents, combined with some aspects of their REE patterns: (1) almost no Eu/Eu* anomaly (0.87–0.91) and (2) high $(La/Lu)_N$ or $(Ce/Yb)_N$ ratios, resembling those of apatite from carbonatites (Belousova et al., 2002), especially the more enriched apatite from the 111658 lherzolite (Table 1). The most relevant difference of apatite from carbonatites is in the halogen contents expressed by the high Cl/F ratio of apatite from El Aprisco xenoliths (1–13), which is clearly at odds with that of carbonatite apatite (typically below 0.05, Chakhmouradian et al., 2017). Nevertheless, the halogen contents of apatite from El Aprisco xenoliths are common in metasomatic apatite-A in peridotites (Fig. 3) (O'Reilly and Griffin, 2000). Likewise, the carbonate content in studied apatites (0.8–2.0 wt%, Table 1) is in the range of chlorapatite-A (O'Reilly and Griffin, 2000).

The in situ Sr-Nd isotopic data obtained for apatite in the 111659 wehrlite yielded a signature similar to that of the Calatrava volcanic rocks, showing a high averaged εNd and a low $^{87}Sr/^{86}Sr$ ratio (FOZO or HIMU composition), although Nd isotopic heterogeneity is significant in apatite crystals (Fig. 4).

GEOCHRONOLOGICAL DATA

Ar-Ar Dating

Ar-Ar data on the mafic megacrysts from the basaltic lavas give ages in the range of other Calatrava volcanic rocks. Amphibole from the El Aprisco volcano (megacryst 114404, Table 2) does not yield a plateau age but a clustering of final steps at around 2.8 ± 0.1 Ma can be taken as the best estimate of the melilitite emplacement age (Data Repository Fig. DR2). Two replicates of the amphibole 111653 megacryst from the Cerro Pelado scoria cone yielded plateau ages of 1.59 ± 0.07 and 1.80 ± 0.06 Ma, whereas the phlogopite 114403 megacryst from the same volcano (Table 2) yielded a good plateau age of 2.23 ± 0.04 Ma (Data Repository Fig. DR3). The phlogopite being slightly older than the amphibole seems to be of more geological significance due to the absence of excess argon in this sample.

Ar-Ar analyses were conducted for metasomatic amphiboles in two peridotite xenoliths from the El Aprisco maar (Table 2). Neither yielded

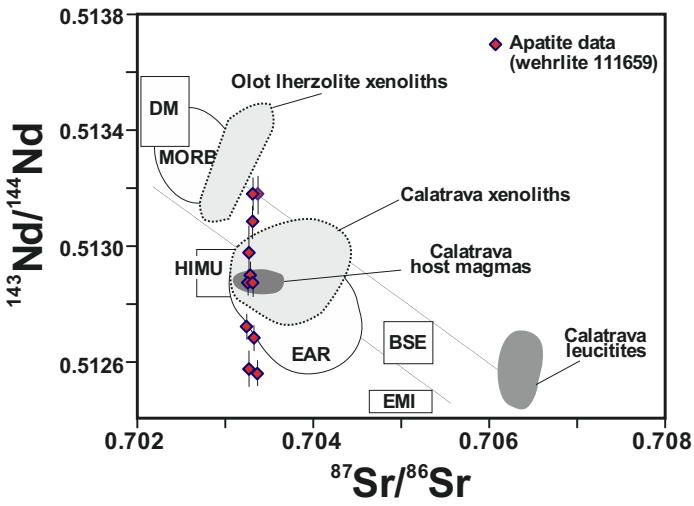

Figure 4. $^{143}Nd/^{144}Nd$ vs $^{87}Sr/^{86}Sr$ diagram for apatite of wehrlite 111659 from El Aprisco. Uncertainty of measurements is included in the symbol size. Mantle-end members (depleted mantle [DM], mid-ocean-ridge basalt [MORB], high μ [μ = $^{238}U/^{204}Pb$ = HIMU], bulk silicate earth [BSE], enriched mantle type 1 [EMI]) are from Zindler and Hart (1986). European Asthenospheric Reservoir (EAR) after Downes et al. (2003). Calatrava leucitite field (ultrapotassic magmatism) is from López-Ruiz et al. (2002) and unpublished data. Other data taken from Villaseca et al. (2010).

plateau ages because they are affected by excess argon. Inverse isochron plots for these samples show trapped component compositions different from those of atmospheric argon. The amphibole of the lherzolite 111658 sample (with accessory apatite) yielded an integrated age of 10.2 ± 0.9 Ma, whereas amphibole from wehrlite 111657 yielded an integrated age of 21.2 ± 0.2 Ma. When only considering final steps (after release of most of the excess argon), ages of 3.9–15.7 Ma, respectively, are obtained (Data Repository Fig. DR2; Table 2). These poorly constrained ages, based on a very restricted number of steps, can be regarded merely as an indication of amphibole formation during metasomatic events before entrainment of the xenolith by the volcanic magma.

U-Pb Dating

Twenty-seven spot analyses were performed on apatite crystals (wehrlite sample 111659), and 24 of these analyses were used for age calculation employing the Tera-Wasserburg concordia approach, which failed to yield a reliable lower intercept age (33 ± 34 Ma; MSWD = 1.2). However, a weighted average of ^{207}Pb-corrected ages approach, which used all 27 analyses, gave the age of 29.0 ± 6.3 Ma with a good MSWD value of 0.22 (Fig. 5). This age was considered to be the most reliable estimate for the timing of metasomatic events forming these apatites.

Only 12 analyses were possible for the lherzolite 111658 due to apatite scarcity and small grain sizes. The Tera-Wasserburg concordia lower intercept age of 121 ± 34 Ma (MSWD = 2.7) and weighted average ^{207}Pb-corrected age of 118.1 ± 9.4 Ma (MSWD = 0.29) (Fig. 5) are values suggesting an old Cretaceous metasomatic event, much older than the one that formed the associated amphibole (~3.9 Ma).

DISCUSSION

Nature of Metasomatic Events

Studied peridotite xenoliths from the El Aprisco show a significant modal metasomatism (González-Jiménez et al., 2014). The most metasomatized peridotites (wehrlites and lherzolites of Group 1) have high

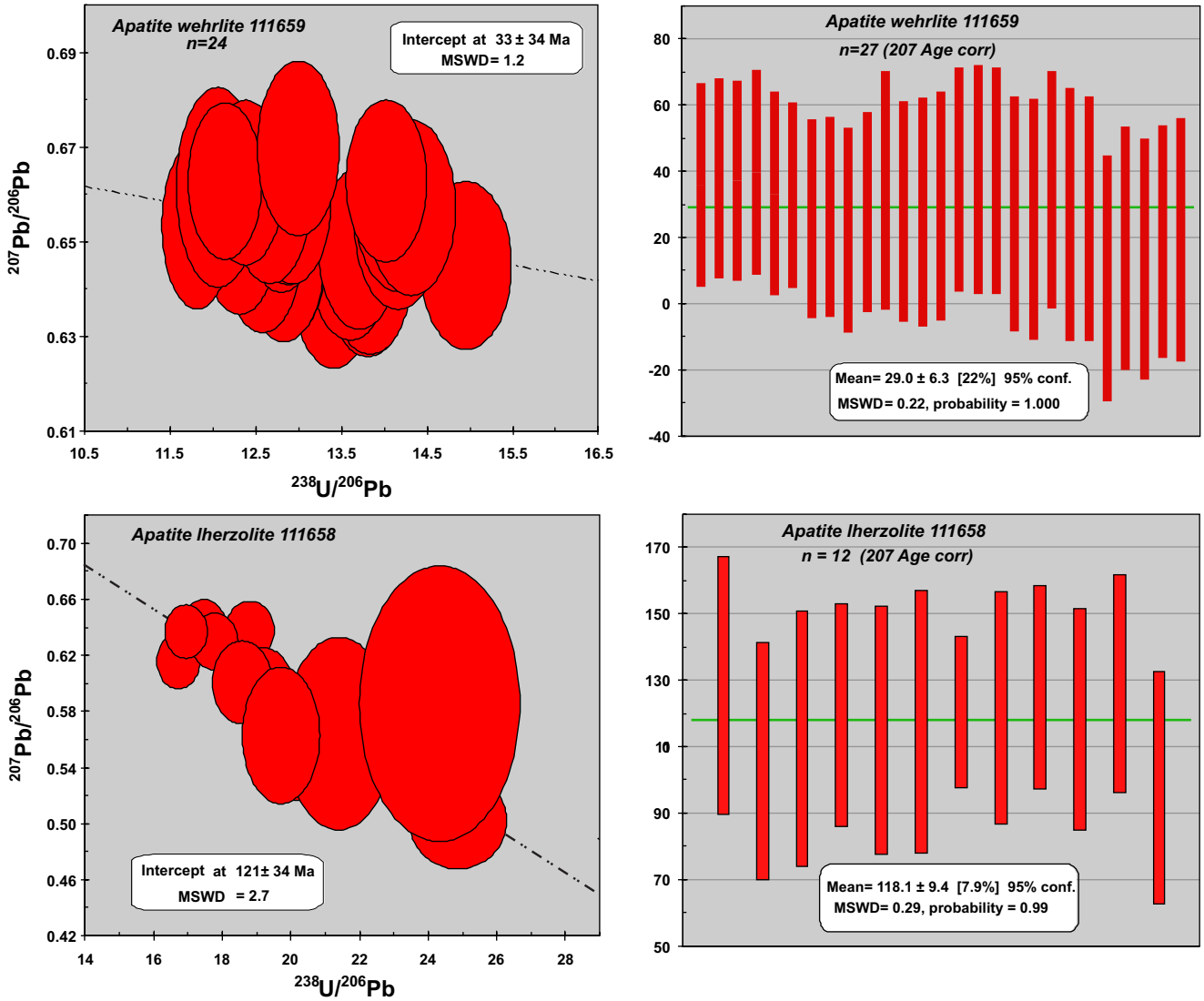

Figure 5. Tera-Wasserburg concordia diagrams (left column) and weighted average ^{207}Pb corrected ages (right column) for the apatite-bearing dated peridotite xenoliths from El Aprisco. MSWD—mean square of weighted deviates.

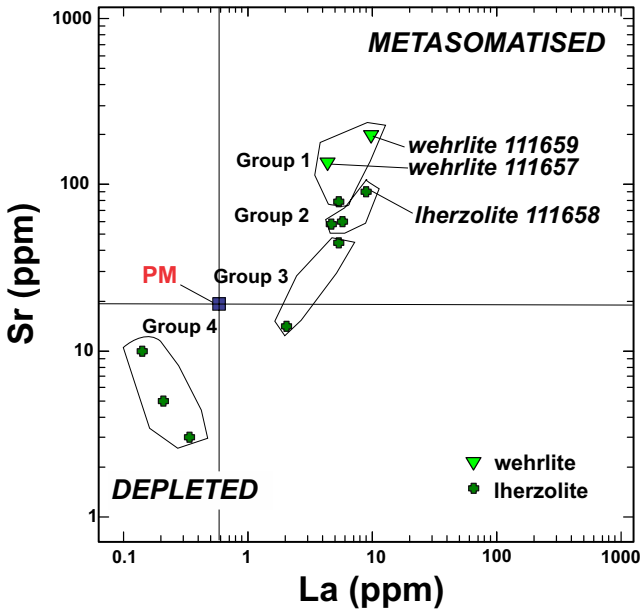

Figure 6. Whole-rock trace-element contents of the different groups of peridotite xenoliths from El Aprisco maar (chemical data from González-Jiménez et al., 2014). Primordial mantle (PM) values after McDonough and Sun (1995).

whole-rock contents of LREE, Nb, Zr, and Sr (Fig. 6), and their clinopyroxenes have low Ti/Eu ratios, indicative of metasomatism by a carbonate-rich agent (Fig. 7). Apatite-poor lherzolite 111658 also has high whole-rock LREE, LILE (Sr, Ba, Rb), Nb, and Zr contents plotting close to the chemical field of Group 1 xenoliths in some diagrams (Fig. 6). Moreover, clinopyroxene in this lherzolite shows low Ti/Eu and high La/Yb values (Fig. 7), also suggesting a carbonate-rich metasomatic agent (Coltorti et al., 1999).

Amphiboles exhibit low Ti/Nb and Zr/Nb ratios in both wehrlites and lherzolite 111658 (always subchondritic <100 and <2, respectively,

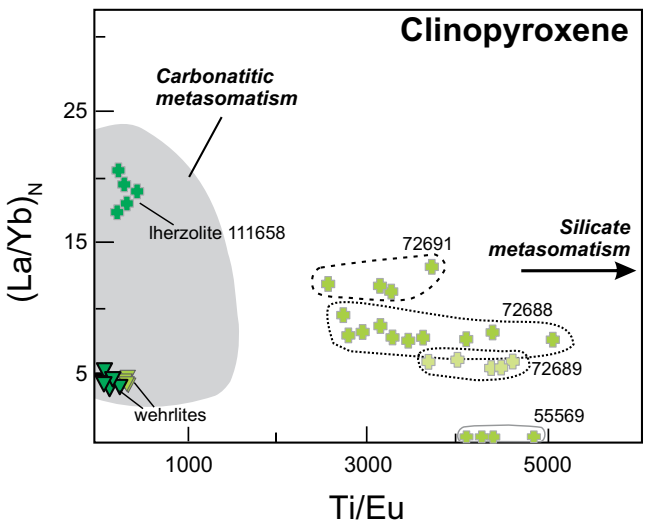

Figure 7. Plot of Ti/Eu vs $(La/Yb)_N$ in clinopyroxene from El Aprisco peridotite xenoliths. Gray symbols are data from other El Aprisco xenoliths (González-Jiménez et al., 2014). Fields for carbonatitic and silicate metasomatism are after Coltorti et al. (1999).

Tables 1 and 5), which suggests crystallization from melt/fluids extracted from mantle domains typical of intraplate settings (Coltorti et al., 2007b). Amphibole composition is consistent with the carbonate-rich silica-undersaturated metasomatism identified from clinopyroxene chemistry.

More information on the chemical characteristics of the metasomatic agents can be derived by calculating the composition of melts in equilibrium with metasomatic phases: clinopyroxene, amphibole, and apatite. We have used clinopyroxene and amphibole K_D's (partition coefficient for mineral-melt equilibria) of basaltic systems (Hart and Dunn, 1993; Zack and Brumm, 1998; La Tourrette et al., 1995; McKenzie and O'Nions, 1991). The calculated melts show high LREE, Th-U, and negative anomalies of Zr, Hf, and Ti characteristics of carbonate-rich magmas (Figs. 8 and 9). Melts in equilibrium with metasomatized clinopyroxene and amphibole from wehrlites (Group 1) and from apatite-poor lherzolite 111658 (Group 2) also yielded a significant Nb-Ta depletion, typical of carbonatites, and very different in normalized trace-element patterns from silicate melts from the CVF (Fig. 9).

Calculated melt composition in equilibrium with apatite using carbonatite systems (Dawson and Hinton, 2003; Hammouda et al., 2010) also yielded a trace element pattern similar to that from clinopyroxene. Thus, calculated melts show consistent features of LREE-enriched melts with marked troughs in Nb-Ta, Zr-Hf, and Ti values, common in carbonate-rich liquids (Fig. 8). When using apatite partition coefficients for basaltic systems (Paster et al., 1974; Prowatke and Klemme, 2006), calculated melts show smaller positive Th-U and negative Ta-Nb, Hf-Zr, and Ti anomalies, although they still look like carbonatite melts.

The isotopic Sr-Nd signature of the analyzed metasomatic apatite is similar to alkaline magmas produced in the Atlantic region and in the European circum-Mediterranean area (e.g., Wagner et al., 2003; Lustrino and Wilson, 2007) (Fig. 4). However, significant Nd-isotope heterogeneity in apatite grains (wehrlite 111659), which is up to 12 epsilon units (Table 4), occurring even at the grain scale, suggests an important chemical modification of the old metasomatic apatite. This Nd-isotope heterogeneity contrasts with the homogeneity of major and trace element compositions and the Sr-isotope signatures of apatite crystals. The lack of isotopic equilibrium between minerals of mantle xenoliths is not uncommon (e.g., Menzies et al., 1987; Raffone et al., 2009). The presence of a network of infiltrating (zeolitized) glass veins close to studied apatite crystals (Fig. 2B) suggests a significant percolative metasomatic agent affecting apatite in later stages. The vein network probably results from alkaline silica-undersaturated melt/fluids generated during Neogene magmatic events, as Nd isotopic heterogeneity in the studied apatite (from MORB to EM-I) encompasses values found in the Iberian Cenozoic volcanism, for example, Olot (NE Spain), and the ultrapotassic leucitites of the Calatrava volcanic field (Fig. 4). However, the question of why Nd-isotope ratios are modified in the absence of any other appreciable chemical modification in the apatite crystal awaits further investigation.

Correlation of Metasomatic Ages with Volcanic Events

In situ U-Pb dating of apatite, as reported herein, is obtained using the inherently high spatial resolution and high-precision LA-ICP-MS technique. Due to the limited number of apatite grains available in some samples, a larger data set would be desirable in future studies to better constrain ages obtained during this research. On the other hand, Ar-Ar geochronology on amphibole had its own challenges due to the presence of excess argon and the potential for open versus closed system behavior (Kelley and Wartho 2000), which resulted in complicated age data being obtained. Assuming closed system behavior for argon in the lithospheric source region, the maximum Ar ages reported herein indicate that

TABLE 5. SUMMARY OF METASOMATIC FEATURES OF PERIDOTITE XENOLITHS FROM THE EL APRISCO MAAR

Sample	Group*	Lithology	Metasomatic features							Comments
			Mineral (modal in %)	$(Ti/Eu)_{cpx}$	$(Th/Nb)_{cpx}$	$(Zr/Nb)_{cpx}$	$(Zr/Nb)_{amph}$	$(Ti/Nb)_{amph}$	Agent	Age (Ma)	
111659	1	W	Apatite (0.3)						CO_3-rich	**29**	Eocene to Miocene carbonatites in the CiMACI
			Amphibole (15)				0.8	20	"		
			Clinopyroxene (28)	220	0.4	85			"		
111657	1	W	Amphibole (18)				1.3	30	"	**15.7**	Miocene carbonatites in the CiMACI
			Clinopyroxene (12)	180	0.2	96			"		
111658	2	L	Apatite (0.01)						"	**118**	Cretaceous carbonatite magmatism in the CiMACI
			Amphibole (5)				0.3	80	"	**3.9**	Calatrava host-magmatism?
			Clinopyroxene (5)	315	1	0.8			"		
72691	2	L	Amphibole (0.5)				15	3500	Subduction		Subduction-related (2)
			Clinopyroxene (10)	3200	205	150			"		
72688	3	L	Amphibole (0.3)				79	12500	Subduction		Old subduction event? (1)
			Clinopyroxene (15)	3450	290	810			"		
55569	4	L	Amphibole (0.01)								
			Clinopyroxene (13)	4500	10	620			Subduction		Subduction-related (2)

Note: W—wehrlite; L—lherzolite; CO_3-rich—carbonatite or carbonated silicate alkaline melt; Subduction—silica-rich not alkaline melt; (1)—Villaseca et al. (2010); (2)—González-Jiménez et al. (2014); CiMACI—Circum-Mediterranean Anorogenic Cenozoic Igneous (Lustrino and Wilson, 2007).
*Xenolith groups of El Aprisco center after González-Jiménez et al. (2014).

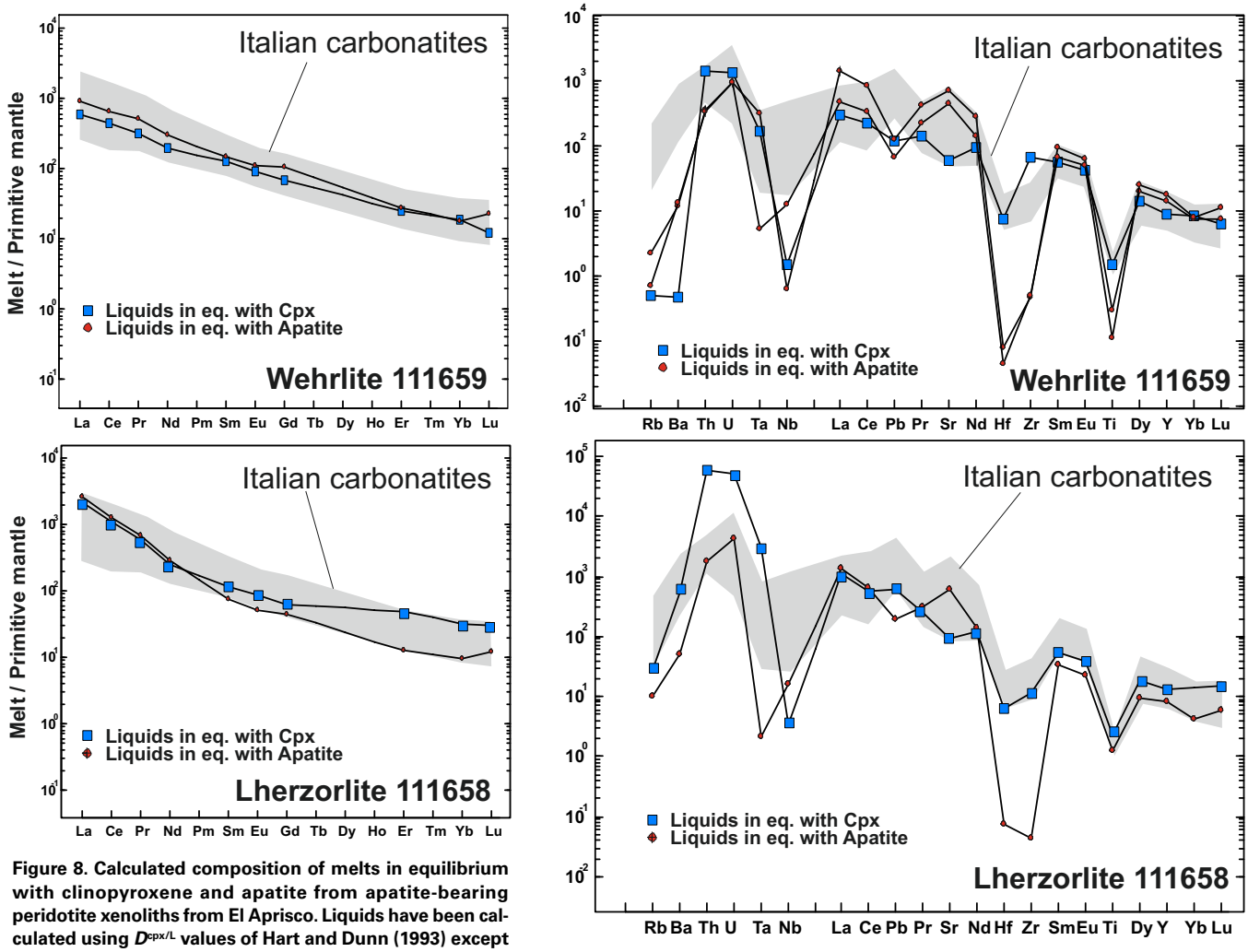

Figure 8. Calculated composition of melts in equilibrium with clinopyroxene and apatite from apatite-bearing peridotite xenoliths from El Aprisco. Liquids have been calculated using $D^{cpx/L}$ values of Hart and Dunn (1993) except for Rb, Th, U, Ta, Eu, and Gd (Zack and Brumm, 1998), and $D^{ap/L}$ values of Hammouda et al. (2010). The compositional range of Italian carbonatites is from Stoppa and Sciazza (2013). Normalizing values are from McDonough and Sun (1995).

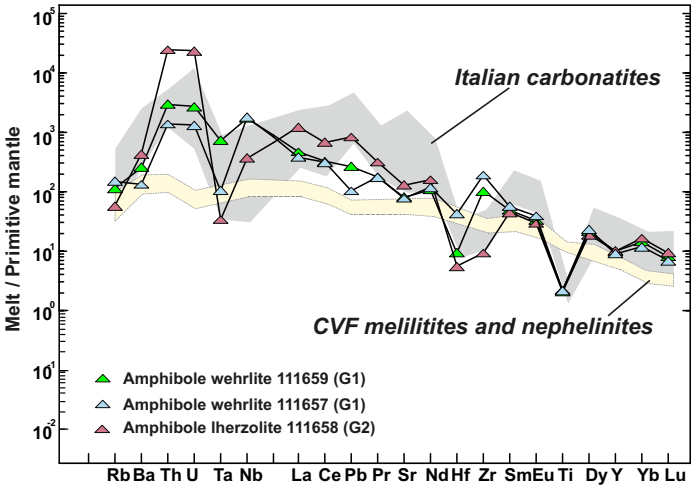

Figure 9. Calculated composition of melts in equilibrium with amphibole from apatite-bearing peridotite xenoliths from Calatrava volcanic field (CVF), El Aprisco. Melts were calculated using $D^{amph/L}$ values of La Tourrette et al. (1995), except for Sm, Eu, Dy, Yb, and Ti (McKenzie and O'Nions, 1991). The compositional range of Italian carbonatites is from Stoppa and Sciazza (2013), whereas the composition of the Calatrava host volcanic rocks (melilitites and nephelinites) are from Cebriá and López-Ruiz (1995). Normalizing values are from McDonough and Sun (1995).

metasomatic interactions in the studied samples cannot be attributed to a single event, given that ages recorded from apatite are much older than those obtained from the amphibole samples (Table 5). For these reasons, we believe our geochronological data to be sufficiently robust to initiate discussion of the correlation between metasomatic events undergone by Calatrava peridotites and coeval magmatism recorded in the Iberian microplate, as well as its implications for geodynamic models pertaining to the circum-Mediterranean province.

The Calatrava volcanic field was formed during two separate stages of magmatism. The oldest one was a minor ultrapotassic event at around 8.7–6.4 Ma, whereas the youngest was the main Na-rich alkaline event occurring from 4.7 to 0.7 Ma (e.g., Ancochea, 1982). Our Ar-Ar geochronological data on mafic megacrysts from basaltic magmas give ages in the range of other Calatrava volcanic rocks: 2.8 ± 0.1 Ma for amphibole from the El Aprisco volcano, and 2.2 ± 0.1–1.8 ± 0.1 Ma for phlogopite and amphibole, respectively, from the nearby Cerro Pelado volcano (Table 2; Data Repository Fig. DR3). These ages are within the timeframe of 4.7 to around 0.7 Ma reported for similar alkaline volcanic rocks of the Calatrava field in previous studies (Ancochea, 1982; Herrero-Hernández et al., 2015). However, some previous K-Ar dating of mafic megacrysts of the olivine nephelinite from the Cerro Pelado volcano yielded ages of 4.6 ± 0.7 (amphibole) to 3.4 ± 0.4 Ma (phlogopite) (Ancochea, 1982), a slightly older range than the dating obtained in this study.

Most dated metasomatic minerals have yielded ages greater than the known period of volcanic activity in the Calatrava field (Table 5). Nevertheless, interstitial peridotite amphiboles have estimated maximum Ar-Ar ages of 3.9 (lherzolite Group 2) to 15.7 Ma (wehrlite Group 1), almost overlapping the time of alkaline eruptions in the Calatrava volcanism.

In contrast, U-Pb ages obtained for metasomatic apatites indicate the existence of much older metasomatic events in the mantle beneath central Spain. The measured ages range from Aptian to Rupelian, indicating a previously unknown occurrence of a Cretaceous to Oligocene alkaline magmatism in central Spain. These new geochronological data provide evidence that apatite-forming metasomatic events occurred significantly earlier than the age range of the Calatrava volcanism and also record older stages, as compared to the metasomatic events that produced amphibole in the same peridotite xenolith (Table 5). Therefore, at least three metasomatic events have been identified within the SCLM beneath central Spain in Cretaceous (118 Ma), Oligocene (29 Ma) and Miocene (16–4 Ma) times, but the vestiges of these events in the Iberian microplate are very scarce.

Significance of Magmatic (Metasomatic Imprint) Ages

During the Late Mesozoic to Cenozoic times, Iberia registered several cycles of sporadic intraplate magmatism of alkaline affinity (e.g., Mata et al., 2015).

A first cycle of basic mildly alkaline magmas at 148–140 Ma appears to have been associated with peripheral rift basins in central western Portugal, suggesting a passive-type margin scenario (Mata et al., 2015). Their trace-element compositions combined with Sr-Nd isotopic signatures, close to CHUR values, suggest derivation from a metasomatized lithospheric source (Mata et al., 2015). A unique alkaline basaltic outcrop at the Languedoc volcanic field (SE France) yielded 161 Ma (Dautria et al., 2010), but slightly older Middle Jurassic alkaline volcanism (~176–165 Ma) has been described in the Iberian Range, also considered to be related to passive margin settings (Lago et al., 2004; Cortés and Gómez, 2016).

A second magmatic cycle is described at 94–69 Ma (e.g., Grange et al., 2010), although including age data for the Tore-Madiera (TMR) seamounts and the Morocco (Taourirt), Iberia (Galicia, Pyrenees), and Languedoc areas, might extend this magmatism to a wider interval, i.e., from 105 to 57 Ma (Dautria et al., 2010; Ubide et al., 2014). This second cycle corresponds with more widespread magmatic activity along the ocean-continent transition zone (J-anomaly or Meosozoic peridotite ridge TMR), continental Iberia and the Pyrenees areas, and the Languedoc area in southern France (Fig. 10A), comprising basic magmas more silica-undersaturated than in the previous cycle (e.g., Grange et al., 2010; Dautria et al., 2010). This magmatic event presents unequivocal geochemical affinities to the Common Mantle Reservoir (CMR) or the European Asthenospheric Reservoir typical of the anorogenic circum-Mediterranean area (Grange et al., 2010; Dautria et al., 2010; Ubide, 2013). The following isotopic compositions are typical of the CMR: $^{87}Sr/^{86}Sr$ = 0.7030–0.7037, and $^{143}Nd/^{144}Nd$ = 0.51300–0.51279 (Lustrino and Wilson, 2007). This Late Cretaceous alkaline magmatism is of lithospheric-asthenospheric origin, and some authors suggest a mantle plume component (e.g., Grange et al., 2010).

The third anorogenic magmatic cycle in Iberia is defined as being from 11 Ma to the present time (Ancochea, 2004), although orogenic calc-alkaline magmatism is slightly older in SE Spain (up to 18.5 Ma, Duggen et al., 2004). The third episode includes the studied Calatrava volcanic field with magmatic activity from 7 to 1 Ma. This magmatism is well recorded in continental Western Europe and in the Mediterranean area, and is characterized by Na-rich alkaline magmas, with signatures typical of OIB and a significant HIMU-FOZO component (e.g., Lustrino and Wilson, 2007; Faccena et al., 2010).

When summarizing age data from specific microplates (such as the Iberian plate), magmatic activity seems to be marked by the occurrence of magmatic episodes separated by periods of quiescence (Fig. 11). In contrast, when considering all of Western Europe–North Africa and Central Atlantic seamounts and islands, anorogenic magmatism seems to be more continuous, although scarce (Fig. 10). For instance, the apparent absence of magmatism in Iberia for more than 60 Ma, i.e., from 76 Ma for Portuguese and Catalonian alkaline intrusions (Grange et al., 2010; Ubide, 2013; Ubide et al., 2014) to Neogene intraplate volcanism, may simply reflect incomplete sampling. Indeed, the age reported herein of

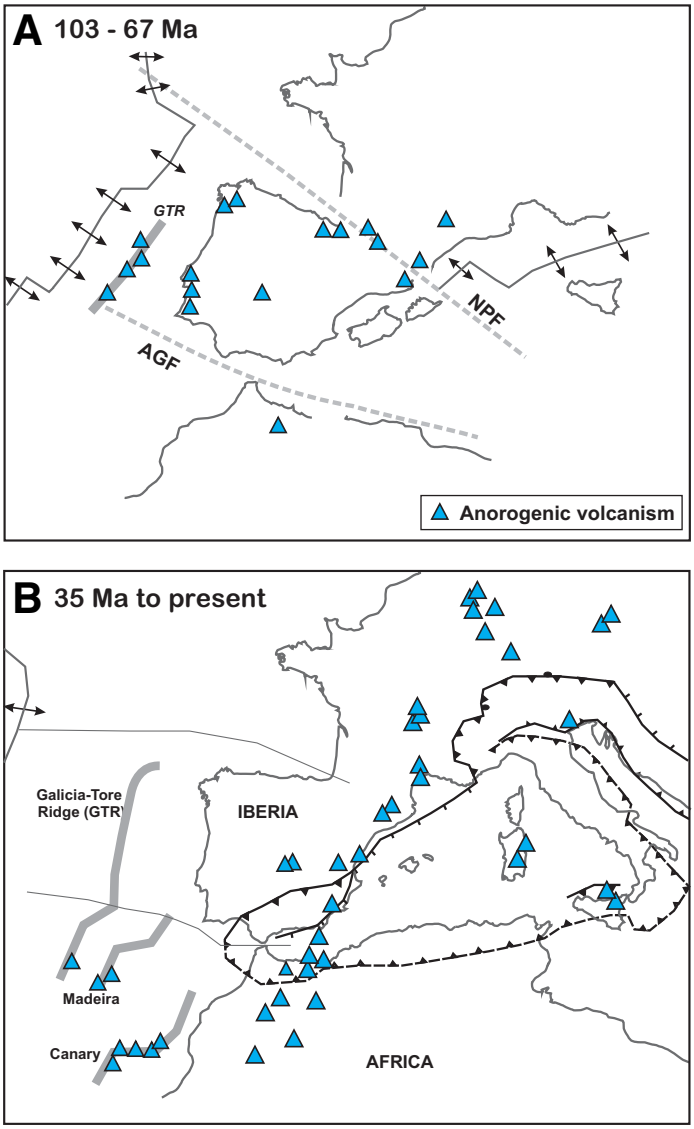

Figure 10. Geological sketch showing the anorogenic magmatism in Iberia and related areas from Cretaceous to Quaternary. (A) The opening of the North-Atlantic and Valais oceans and eastern escape of Iberia with early Pyrenean collisional tectonic features (NPF—North Pyrenean Fault; AGF—Azores-Gibraltar Fault) are based on maps in Schettino and Turco (2011). Alkaline magmatism is recorded in the Galicia-Tore ridge (GTR) and western Portugal (Grange et al., 2010), Morocco (Wagner et al., 2003), NW Spain (Ancochea et al., 1992), Basque country–Pyrenees and Catalonian coastal ranges (Ubide et al., 2014), and Languedoc (Dautria et al., 2010). Cretaceous Calatrava magmatism is included in this data set. (B) Cenozoic alkaline magmatism at the Madeira and Canary ridges, northern Africa and western European countries, are mainly taken from Lustrino and Wilson (2007).

16–29 Ma for the carbonate-rich alkaline magmatism that metasomatized the SCLM below Calatrava (forming wehrlites) fills this temporal gap and is close to the age of carbonatite-silicate magmatism in northern Morocco, at Azrou-Timahdite (35 Ma, Raffone et al., 2009) and at Tamazert (44–35 Ma, Marks et al., 2009; Bouabdellah et al., 2010; Fig. 11).

The Late Cretaceous age found in metasomatic apatite from the lherzolite 111658 sample not only implies that this sporadic second magmatic cycle occurs in many parts of the Iberian peninsula, having first been reported from central Spain, but also suggests that a significant part of deep mantle-derived magmatic activity leaves no trace in overlying crustal levels. Percolating melts and fluids within the lithospheric mantle have little chance to progress upwards and reach the upper crust or even the surface to form volcanic rocks. Indeed, it is suggested that less than 10% of the budget of a magmatic cycle yields volcanic deposits, in contrast to the dominant plutonic counterpart trapped at greater depths (e.g., Perfit and Davidson, 2000). Recently, estimates of plutonic-to-volcanic ratios have increased to values up to 65:1 in subduction environments with high magmatic fluxes (de Silva and Kay, 2018), indicating that most melts of magmatic plumbing systems never reach the surface.

Geodynamic Implications of Cretaceous–Cenozoic Magmatism in Central Spain

In Iberia, the breakup of Pangea is manifested mainly by dyke intrusions (e.g., Messejana-Plasencia dyke, Dunn et al., 1998; Cebriá et al., 2003) forming part of a tholeiitic magmatic cycle at 202–198 Ma, which is coeval with the beginning of the Central Atlantic opening as a part of the Central Magmatic Province (e.g., Marzoli et al., 1999). Subsequently, the Iberian microplate was subjected to a complex evolution mostly constrained by the relative motion of the surrounding European and African lithospheric plates and the progressive opening of the Atlantic Ocean.

During the Mesozoic, two alkaline magmatic cycles in the Iberian microplate generated minor volumes of mildly alkaline volcanic rocks at the Jurassic–Cretaceous transition into more abundant Late Cretaceous alkaline massifs (Mata et al., 2015) (Fig. 11). The geological setting for these magmatic events is described as an extensional regime linked to the opening of the North Atlantic Ocean evolving from rift-related small intracontinental basins toward major involvement of mantle thermal anomalies (plumes?) related to the motion of the Iberian plate. The opening of the Bay of Biscay and allied rotation of Iberia with respect to Europe led to the emplacement of more silica-undersaturated rocks toward the end of this cycle (e.g., Grange et al., 2010; Ubide et al., 2014).

Data from the three magmatic alkaline cycles in Iberia and adjacent areas suggest a progression over time of several features that are significant for the evolving geodynamical setting of the Western Europe: (i) magmatism becomes more silica-undersatured with time, (ii) there is a broad geographical evolution toward (south)-eastern magma emplacement, and (iii) magma flux from deeper mantle levels increases (from lithosphere-dominant sources during Mesozoic to major involvement of asthenosphere-derived magmas in the Cenozoic).

The Jurassic–Cretaceous Lusitanian volcanic rocks of the western Iberian margin are moderately alkaline to slightly subalkaline (tholeiitic) basic magmas of lithospheric origin (Mata et al., 2015). During the Late Cretaceous, the magmatism evolves toward more alkaline affinity either in the Pyrenees or in SW Portugal, showing in both areas an evolution to more silica-undersaturated magmas with time (lamprophyres of 79 Ma in the Catalonian Coastal Ranges; Monchique suite of 69 Ma, in SW Portugal). Markedly less alkaline rocks of Iberia have older Late Cretaceous ages: 105–85 Ma in the Basque-Cantabrian basin and the Pyrenees (Ubide et al., 2014), 88–76 Ma in SW Portugal (Grange et al., 2010), and 97–87 Ma in Galicia (Ancochea et al., 1992). The generation of alkaline magmas in the Iberian microplate with HIMU-FOZO signatures occurred during this ultra-alkaline and silica-undersaturated Campanian-Maastrichian sub-episode (Ubide, 2013; Grange et al., 2010). This mantle composition coupled with ultra-alkaline silica-undersaturated magmas is typical of the Cenozoic alkaline magmatism of Iberia in their volcanic fields: e.g., Calatrava (López Ruiz et al., 2002) and Olot (Cebriá et al., 2000). Notably, enriched lithospheric components such as CHUR (Tallante, Beccaluva

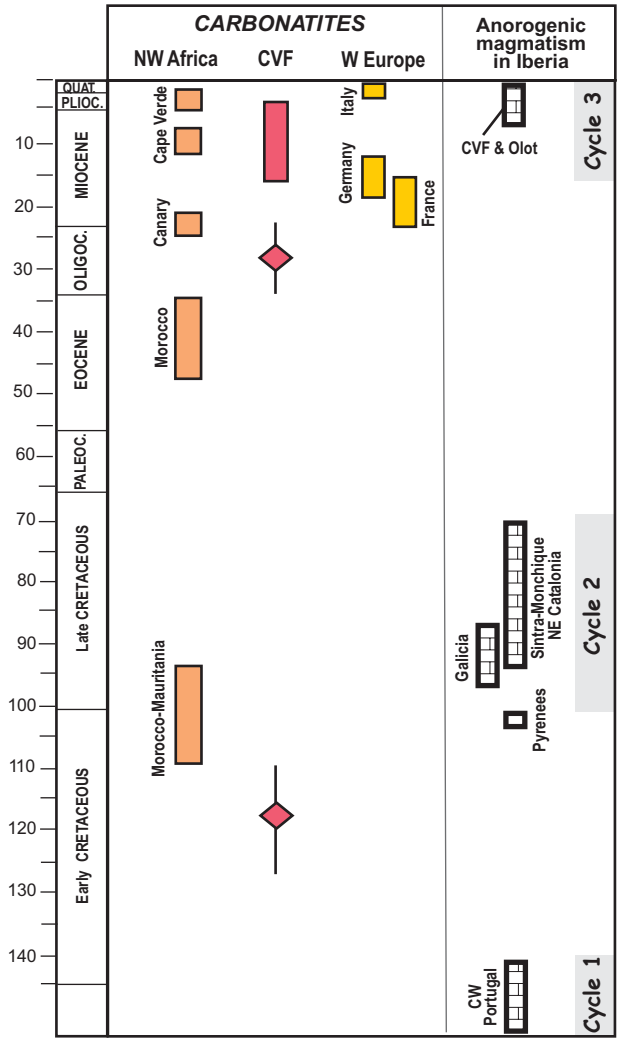

Figure 11. Timing of carbonatitic magmatism from the Western circum-Mediterranean province used in this paper for correlation. It also included the timing of anorogenic magmatism in the Iberian Peninsula, and magmatic cycles after Mata et al. (2015). Geochronological data of the Calatrava volcanic field (CVF) is from this data set. Other references are: Cape Verde (Madeira et al., 2005; Holm et al., 2008, and references therein), Canary (Muñoz et al., 2005), Morocco (Bouabdellah et al., 2010), Morocco-Mauritania (Montero et al., 2016, and references therein), France (Chazot and Mergoil-Daniel, 2012), Germany (Wang et al., 2014), and Italy (Lavecchia et al., 2006).

et al., 2004) or EM1 (leucititic magmas of Calatrava, López Ruiz et al., 2002) are also found in coeval volcanic products from these areas.

A geographical shift toward the SE over time is possible to envisage not only in a broad comparison among the locations of the three alkaline magmatic cycles (Fig. 10) but also when considering its evolution in the different Iberian sectors. During the Late Cretaceous, the described geochemical evolution goes along with a displacement of the magmatism toward eastern (Pyrenees) and southeastern (Portugal) locations. Moreover, the easternmost alkaline volcanic fields in Iberia (Olot, Cofrentes, Tallante) start their activity during the Late Cenozoic (last 10 Ma, López Ruiz et al., 2002). Thus, a migration of magmatism from the Atlantic toward the Mediterranean Iberian margin is evident.

The involvement of the ubiquitous FOZO component in the Iberian OIB-type basalts from Late Cretaceous times introduces important questions of its appearance in intracontinental settings with variable lithospheric sections. First, there is the potential involvement of sub-lithospheric deep mantle sources (the so-called European asthenospheric reservoir, Downes et al., 2003), and second, the possibility of focused upwelling of mantle material by plume-like structures. The scarce, discontinuous, and low volume magmatism that characterizes these alkaline cycles in Iberia and related areas are arguments against plume magmatism (e.g., Mata et al., 2015). This magmatism may have been triggered by mantle flow instabilities from transform faults (as the Tore-Madeira ridge) or small hotspots aligned parallel to the original western limit of the continent-ocean transition zone, during Atlantic opening (as Canary or Cape Verde volcanic lineaments). The onset of the Africa-Eurasia collision, mostly from 45 Ma onwards (e.g., Carminati et al., 2012), produced a more complex scenario for the Iberian plate. Geophysical models of the western Mediterranean indicate a marked lithospheric removal or small-scale convective heterogeneities in the upper mantle related to complex oceanic subduction trajectories (e.g., Faccena et al., 2010; Thurner et al., 2014). Crustal subduction events have occurred during the opening of the Alboran basin (SE Spain, Carminati et al., 2012, and references therein) and others that operate within a mosaic of microplates in the Mediterranean region (e.g., Faccena and Becker, 2010), generating complex small-scale convection associated with retreating slabs (Faccena et al., 2010; Thurner et al., 2014). The delamination of continental margin lithosphere when oceanic crust is consumed by subduction and slab rollback could initiate lithosphere detachment and permit asthenosphere upwelling (e.g., Thurner et al., 2014). This mechanism, combined with accommodation along transform faults, could explain the generation of anorogenic magmas during the Neogene (Melchiorre et al., 2017). A similar scenario is also envisaged in central Iberia where the existence of large Variscan shear bands weakened the crust and facilitated the ascent of underplated material stacked below the Moho boundary during the generation of the CVF (Granja et al., 2015).

CONCLUSION

To our knowledge, this is the first study dating mantle metasomatic minerals using a combination of different methodologies (in situ U-Pb on apatite coupled with Ar-Ar on amphibole separates) on a peridotite suite from a Cenozoic volcanic center within the circum-Mediterranean province. The geochronological data obtained imply that metasomatic interactions in the studied samples cannot be attributed to a single event, but rather successive metasomatic events recording subsequent percolation of ultra-alkaline melts within the subcontinental lithospheric mantle of central Spain over the last 120 Ma. This sporadic percolation of carbonatite or carbonated silicate melts from late Cretaceous to Neogene times occurred in at least three successive stages (Fig. 11). Carbonatites of Eocene to Miocene ages are abundant in the Atlantic islands (Cape Verde, Canary) and NW Africa (e.g., Madeira et al., 2005; Muñoz et al., 2005; Bouabdellah et al., 2010), and also in Cenozoic volcanic fields of Western Europe (Rhine, French Massif Central, Italy) (e.g., Stoppa and Sciazza, 2013; Wang et al., 2014). Correlating the Cretaceous carbonatite signature found in the apatite crystals from peridotite xenolith 111658 of the El Aprisco maar (Table 5) is, however, more difficult as no carbonatitic magmatism of similar age has been recorded in the circum-Mediterranean realm except in northwestern Africa where some few intrusive complexes have been described (e.g., Montero et al., 2016, and references therein). This issue merits further investigation.

Ages recorded from apatite are much older than those from associated amphibole in the studied samples (Table 5). Mantle xenoliths containing

apatite are especially significant when this accessory mineral appears disseminated in the peridotite matrix and is not related to melt pockets or glass veins, as in the studied samples (Fig. 2), suggesting that apatite is not involved in partial melting processes (see also Chazot et al., 1996b). The resistance to melting of this mantle mineral can be used to study old metasomatic events and agents. In our present study, mineral chemistry results indicate carbonated ultra-alkaline signatures for the successive metasomatic imprints (Table 5). This research highlights the possibility of a great age span between metasomatic overprints in the same section of the mantle due to the preservation of relictic metasomatic minerals.

ACKNOWLEDGMENTS

We thank Alfredo Fernández Larios for his assistance with the electron microprobe analyses in the Centro Nacional de Microscopía Electrónica *Luis Bru* (UCM). We greatly appreciate the constructive comments made by Michel Grégoire and Teresa Ubide on a previous version of the manuscript. This work is included in the objectives and supported by the CGL2016–78796 project of the Spanish Ministerio de Ciencia, Innovación y Universidades (MICINN) and the UCM 910492 group. González-Jiménez acknowledges financial support of the Ramón y Cajal Fellowship RYC-2015–17596, granted by the Spanish Ministerio de Economía y Empresa (MINECO).

REFERENCES CITED

Ackerman, L., Walker, R.J., Puchtel, I.S., Pitcher, L., Jelínek, E., and Strnad, L., 2009, Effects of melt percolation on highly siderophile elements and Os isotopes in subcontinental lithospheric mantle: A study of the upper mantle beneath central Europe: Geochimica et Cosmochimica Acta, v. 73, p. 2400–2414, https://doi.org/10.1016/j.gca.2009.02.002.

Alard, O., Griffin, W.L., Pearson, N.J., Lorand, J.P., and O'Really, S.Y., 2002, New insights into the Re-Os systematics of sub-continental lithospheric mantle from in situ analysis of sulphides: Earth and Planetary Science Letters, v. 203, p. 651–663, https://doi.org/10.1016/S0012-821X(02)00799-9.

Ancochea, E., 1982, Evolución espacial y temporal del volcanismo reciente de España Central [Ph.D. thesis]: Complutense University, Madrid (203/83), 675 p.

Ancochea, E., 2004, La region volcánica del Campo de Calatrava, *in* Vera, J.A., ed., Geología de España: Madrid, SGE-IGME, p. 676–677.

Ancochea, E., Huertas, M.J., Ibarrola, E., and Snelling, N., 1992, Diques basálticos en las proximidades de Orense: Evidencia de actividad magmática Cretácica en el noroeste de la Península Ibérica: Revista de la Sociedad Geológica de España, v. 5, p. 65–71.

Amelin, Y., and Zaitsev, A.N., 2002, Precise geochronology of phoscorites and carbonatites: The critical role of U-series disequilibrium in age interpretations: Geochimica et Cosmochimica Acta, v. 66, p. 2399–2419, https://doi.org/10.1016/S0016-7037(02)00831-1.

Bailey, K., Garson, M., Kearns, S., and Velasco, A.P., 2005, Carbonate volcanism in Calatrava, central Spain: A report of initial findings: Mineralogical Magazine, v. 69, p. 907–915.

Beccaluva, L., Bianchini, G., Bonadiman, C., Siena, F., and Vaccaro, C., 2004, Coexisting anorogenic and subduction-related metasomatism in mantle xenoliths from the Betic Cordillera (southern Spain): Lithos, v. 75, p. 67–87, https://doi.org/10.1016/j.lithos.2003.12.015.

Belousova, E.A., Griffin, W.L., O'Reilly, S.Y., and Fisher, N.I., 2002, Apatite as an indicator mineral for mineral exploration: Trace-element compositions and their relationship to host rock type: Journal of Geochemical Exploration, v. 76, p. 45–69, https://doi.org/10.1016/S0375-6742(02)00204-2.

Bianchini, G., Beccaluva, L., Bonadiman, C., Nowell, G.M., Pearson, D.G., Siena, F., and Wilson, M., 2010, Mantle metasomatism by melts of HIMU piclogite components: New insights from Fe-rich lherzolite xenoliths (Caltrava volcanic District, central Spain), *in* Coltorti, M., Downes, H., Grégoire, M., and O'Reilly, S., eds., Petrological Evolution of the European Lithospheric Mantle: Geological Society, London, Special Publications 337, p. 107–124, https://doi.org/10.1144/SP337.6.

Bouabdellah, M., Hoernle, K., Kchit, A., Duggen, S., Hauff, F., Klügel, A., Lowry, D., and Beaudoin, G., 2010, Petrogenesis of the Eocene Tamazert continental carbonatites (central High Atlas, Morocco): Implications for a common source for the Tamazert and Canary and Cape Verde islands carbonatites: Journal of Petrology, v. 51, p. 1655–1686, https://doi.org/10.1093/petrology/egq033.

Carminati, E., Lustrino, M., and Doglioni, C., 2012, Geodynamic evolution of the central and western Mediterranean: Tectonics vs. igneous petrology constraints: Tectonophysics, v. 579, p. 173–192, https://doi.org/10.1016/j.tecto.2012.01.026.

Cebriá, J.M., and López-Ruiz, J., 1995, Alkali basalts and leucitites in an extensional intracontinental plate setting: The late Cenozoic Calatrava Volcanic Province (central Spain): Lithos, v. 35, p. 27–46, https://doi.org/10.1016/0024-4937(94)00027-Y.

Cebriá, J.M., López-Ruiz, J., Doblas, M., Oyarzun, R., Hertogen, J., and Benito, R., 2000, Geochemistry of the Quaternary alkali basalts of Garrotxa (NE volcanic province, Spain): A case of double enrichment of the mantle lithosphere: Journal of Volcanology and Geothermal research, v. 102, p. 217–235.

Cebriá, J.M., López-Ruiz, J., Doblas, M., Martins, L.T., and Munha, J., 2003, Geochemistry of the early Jurassic Messejana-Plasencia dyke (Portugal-Spain): Implications on the origin of the Central Atlantic Magmatic Province: Journal of Petrology, v. 44, p. 547–568, https://doi.org/10.1093/petrology/44.3.547.

Cebriá, J.M., Martín-Escorza, C., López-Ruiz, J., Morán-Zenteno, D.J., and Martiny, B.M., 2011, Numerical recognition of alignements in monogenetic volcanic areas: Examples from the Michoacán-Guanajato Volcanic Field in Mexico and Calatrava in Spain: Journal of Volcanology and Geothermal Research, v. 201, p. 73–82, https://doi.org/10.1016/j.jvolgeores.2010.07.016.

Chakhmouradian, A.R., Reguir, E., Zaitsev, A.N., Coüeslan, C., Xu, C., Kynický, J., Mumin, H., and Yang, P., 2017, Apatite in carbonatitic rocks: Compositional variation, zoning, element partitioning and petrogenetic significance: Lithos, v. 274-275, p. 188–213.

Chazot, G., and Mergoil-Daniel, J., 2012, Co-eruption of carbonate and silicate magmas during volcanism in the Limagne graben (French Massif Central): Lithos, v. 154, p. 130–146, https://doi.org/10.1016/j.lithos.2012.06.032.

Chazot, G., Menzies, M.A., and Harte, B., 1996a, Determination of partition coefficients between apatite, clinopyroxene, amphibole, and melt in natural spinel lherzolites from Yemen: Implications for wet melting of the lithosphere mantle: Geochimica et Cosmochimica Acta, v. 60, p. 423–437, https://doi.org/10.1016/0016-7037(95)00412-2.

Chazot, G., Menzies, M.A., and Harte, B., 1996b, Silicate glasses in spinel lherzolites from Yemen: origin and chemical composition: Chemical Geology, v. 134, p. 159–179, https://doi.org/10.1016/S0009-2541(96)00086-1.

Chew, D.M., Sylvester, P.J., and Tubrett, M.N., 2011, U-Pb and Th-Pb dating of apatite by LA-ICPMS: Chemical Geology, v. 280, p. 200–216, https://doi.org/10.1016/j.chemgeo.2010.11.010.

Coltorti, M., Bonadiman, C., Hinton, R.W., Siena, F., and Upton, B.G.J., 1999, Carbonatite metasomatism of the oceanic upper mantle: evidence from clinopyroxenes and glasses in ultramafic xenoliths of Grande Comore, Indian Ocean: Journal of Petrology, v. 40, p. 133–165, https://doi.org/10.1093/petroj/40.1.133.

Coltorti, M., Bonadiman, C., Faccini, B., Ntaflos, T., and Siena, F., 2007a, Slab melt and intraplate metasomatism in Kapfenstein mantle xenoliths (Styria Basin, Austria): Lithos, v. 94, p. 66–89, https://doi.org/10.1016/j.lithos.2006.07.003.

Coltorti, M., Bonadiman, C., Faccini, B., Grégoire, M., O'Reilly, S.Y., and Powell, W., 2007b, Amphiboles from suprasubduction and intraplate lithospheric mantle: Lithos, v. 99, p. 68–84, https://doi.org/10.1016/j.lithos.2007.05.009.

Cortés, J.E., and Gómez, J.J., 2016, Middle Jurassic volcanism in a magmatic-rich passive margin linked to the Caudiel Fault Zone (Iberian Range, East of Spain): Biostratigraphical dating: Journal of Iberian Geology, v. 42, p. 335–354, https://doi.org/10.5209/JIGE.54667.

Coulson, I.M., Villeneuve, M.E., Dipple, G.M., Duncan, R.A., Russell, J.K., and Mortensen, J.K., 2002, Time-scales of assembly and thermal history of a composite felsic pluton: Constraints from the Emeral Lake area, northern Canadian Cordillera, Yukon: Journal of Volcanology and Geothermal Research, v. 114, p. 331–356, https://doi.org/10.1016/S0377-0273(01)00294-3.

Dautria, J.M., Liotard, J.M., Bosch, D., and Alard, O., 2010, 160 Ma of sporadic basaltic activity on the Languedoc volcanic line (southern France): A peculiar case of lithospheric-asthenospheric interplay: Lithos, v. 120, p. 202–222, https://doi.org/10.1016/j.lithos.2010.04.009.

Dawson, J., and Hinton, R., 2003, Trace-element content and partitioning in calcite, dolomite, and apatite in carbonate, Phalaborwa, South Africa: Mineralogical Magazine, v. 67, p. 921–930, https://doi.org/10.1180/0026461036750151.

de Silva, S.L., and Kay, S.M., 2018, Turning up the Heat: High-flux Magmatism in the Central Andes: Elements, v. 14, p. 245–250, https://doi.org/10.2138/gselements.14.4.245.

Downes, H., Reichow, M.K., Mason, P.R.D., Beard, A.D., and Thirlwall, M.F., 2003, Mantle domains in the lithosphere beneath the French Massif Central: Trace element and isotopic evidence from mantle clinopyroxenes: Chemical Geology, v. 200, p. 71–87, https://doi.org/10.1016/S0009-2541(03)00126-8.

Downes, H., de Vries, C., and Wittig, N., 2015, Hf-Zr anomalies in clinopyroxene from mantle xenoliths from France and Poland: Implications for Lu-Hf dating of spinel peridotite lithospheric mantle: International Journal of Earth Sciences, v. 104, p. 89–102, https://doi.org/10.1007/s00531-014-1074-x.

Duggen, S., Hoernle, K., van der Bogaard, P., and Harris, C., 2004, Magmatic evolution of the Alboran region: The role of subduction in forming the western Mediterranean and causing the Messinian Salinity Crisis: Earth and Planetary Science Letters, v. 218, p. 91–108, https://doi.org/10.1016/S0012-821X(03)00632-0.

Dunn, A.M., Reynolds, P.H., Clarke, D.B., and Ugidos, J.M., 1998, A comparison of the age and composition of the Shelburne dyke, Nova Scotia, and the Messejana dyke, Spain: Canadian Journal of Earth Sciences, v. 35, p. 1110–1115, https://doi.org/10.1139/e98-058.

Faccenna, C., and Becker, T.W., 2010, Shaping mobile belts by small-scale convection: Nature, v. 465, p. 602–605.

Faccena, C., Becker, T.W., Lallemand, S., Lagabrielle, Y., Funiciello, F., and Piromallo, C., 2010, Subduction-triggered magmatic pulses: A new class of plumes?: Earth-Science Reviews, v. 299, p. 54–68.

González-Jiménez, J.M., Villaseca, C., Griffin, W.L., Belousova, E., Konc, Z., Ancochea, E., O'Reilly, S.Y., Pearson, N., Garrido, C., and Gervilla, F., 2013, The architecture of the European-Mediterranean Lithosphere: A synthesis of the Re-Os evidence: Geology, v. 41, p. 547–550, https://doi.org/10.1130/G34003.1.

González-Jiménez, J.M., Villaseca, C., Griffin, W.L., O'Reilly, S.Y., Belousova, E., Ancochea, E., and Pearson, N., 2014, Significance of ancient sulfide PGE and Re-Os signatures in the mantle beneath Calatrava, Central Spain: Contributions to Mineralogy and Petrology, v. 168, p. 1047, https://doi.org/10.1007/s00410-014-1047-x.

Granet, M., Wilson, M., and Achauer, U., 1995, Imaging a mantle plume beneath the French Massif Central: Earth and Planetary science Letters, v. 136, p. 281–296.

Grange, M., Scharer, U., Merle, R., Girardeau, J., and Cornen, G., 2010, Plume-lithosphere interaction during migration of Cretaceous alkaline magmatism in SW Portugal: Evidence from U-Pb ages and Pb-Sr-Hf isotopes: Journal of Petrology, v. 51, p. 1143–1170, https://doi.org/10.1093/petrology/egq018.

Granja, J.L., Vegas, R., Sentre, M.A., Muñoz-Martín, A., and Sainz-Maza, S., 2015, Gravity modeling of the lithosphere in the Calatrava Volcanic Province (Spain): Geodynamic implications: Journal of Iberian Geology, v. 41, p. 233–252.

Griffin, W.L., Powell, W.J., Pearson, N.J., and O'Reilly, S.Y., 2008, GLITTER: Data reduction software for laser ablation ICP-MS, *in* Sylvester, P., ed., Laser Ablation ICP-MS in the Earth

Sciences: Current Practices and Outstanding Issues: Mineralogical Association of Canada, Short Course Series, v. 40, p. 308–311.

Hammouda, T., Chantel, J., and Devidal, J.L., 2010, Apatite solubility in carbonatitic liquids and trace element partitioning between apatite and carbonatite at high pressure: Geochimica et Cosmochimica Acta, v. 74, p. 7220–7235, https://doi.org/10.1016/j.gca.2010.09.032.

Hart, S.R., and Dunn, T., 1993, Experimental cpx/melt partitioning of 24 trace element: Contributions to Mineralogy and Petrology, v. 113, p. 1–8, https://doi.org/10.1007/BF00320827.

Herrero-Hernández, A., López-Moro, F.J., Gallardo-Millán, J.L., Martín-Serrano, A., and Gómez-Fernández, F., 2015, Volcanism-sedimentation interaction in the Campo de Calatrava Volcanic Field (Spain): A magnestostratigraphic and geochronological study: International Journal of Earth Sciences, v. 104, p. 103–122, https://doi.org/10.1007/s00531-014-1053-2.

Holm, P.M., Grandvuinet, T., Friis, J., Wilson, J.R., Barker, A.K., and Plesner, S., 2008, An ^{40}Ar-^{39}Ar study of the Cape Verde hot spot: Temporal evolution in a semi-stationary plate environment: Journal of Geophysical Research, v. 113, B08201, https://doi.org/10.1029/2007JB005339.

Hopp, J., Trielof, M., Brey, G.P., Woodland, A.B., Simon, N.S.C., Wijbrans, J.R., Siebel, W., and Reitter, E., 2008, ^{40}Ar/^{39}Ar-ages of phlogopite in mantle xenoliths from South African kimberlites: Evidence from metasomatic mantle impregnation during the Kibaran orogenic cycle: Lithos, v. 106, p. 351–364, https://doi.org/10.1016/j.lithos.2008.09.001.

Humphreys, E.R., Bailey, K., Hawkesworth, C.J., Wall, F., Najorka, J., and Rankin, A.H., 2010, Aragonite in olivine from Calatrava, Spain: Evidence for mantle carbonatite melts from >100 km depth: Geology, v. 38, p. 911–914, https://doi.org/10.1130/G31199.1.

Ionov, D.A., Griffin, L.W., and O'Reilly, S.Y., 1997, Volatile-bearing minerals and lithophile trace elements in the upper mantle: Chemical Geology, v. 141, p. 153–184, https://doi.org/10.1016/S0009-2541(97)00061-2.

Jackson, S.E., Pearson, N.J., Griffin, W.L., and Belousova, E.A., 2004, The application of laser ablation-inductively coupled plasma-mass spectrometry to in situ U-Pb zircon geochronology: Chemical Geology, v. 211, p. 47–69, https://doi.org/10.1016/j.chemgeo.2004.06.017.

Kelley, S.P., and Wartho, J.A., 2000, Rapid kimberlite ascent and significance of Ar-Ar ages in xenolith phlogopites: Science, v. 289, p. 609–611, https://doi.org/10.1126/science.289.5479.609.

La Tourrette, T., Hervig, R.L., and Holloway, J.R., 1995, Trace element partitioning between amphibole, phlogopite, and basanite melt: Earth and Planetary Science Letters, v. 135, p. 13–30, https://doi.org/10.1016/0012-821X(95)00146-4.

Lago, M., Arranz, E., Gil, A., and Pocoví, A., 2004, Magmatismo asociado, *in* Vera, J.A., ed., Madrid, Geología de España, SGE-IGME, p. 522–525.

Lavecchia, G., Stoppa, F., and Creati, N., 2006, Carbonatites and kamafugites in Italy: Mantle-derived rocks that challenge subduction: Annals of Geophysics, v. 49, p. 389–402.

Lierenfeld, M.B., and Mattsson, H.B., 2015, Geochemistry and eruptive behaviour of the Finca la Nava maar volcano (Campo de Calatrava, south-central Spain): International Journal of Earth Sciences, v. 104, p. 1795–1817, https://doi.org/10.1007/s00531-015-1164-4.

López Ruiz, J., Cebriá, J.M., Doblas, M., Oyarzun, R., Hoyos, M., and Martín, C., 1993, The late Cenozoic alkaline volcanism of the central Iberian Peninsula (Calatrava Volcanic Province, Spain): Intraplate volcanism related to extensional tectonics: Journal of the Geological Society, London, v. 150, p. 915–922.

López-Ruiz, J., Cebriá, J.M., and Doblas, M., 2002, Cenozoic volcanism I: The Iberian peninsula, *in* Gibbons, W., and Moreno, T., eds., The Geology of Spain: Geological Society, London, p. 417–438, https://doi.org/10.1144/GOSPP.17.

Ludwig, K.R., 2003, ISOPLOT/Ex, version 3: A geochronological toolkit for Microsoft Excel: Berkeley Geochronological Center, Special Publication 4.

Lustrino, M., and Wilson, M., 2007, The circum-Mediterranean anorogenic Cenozoic igneous province: Earth-Science Reviews, v. 81, p. 1–65, https://doi.org/10.1016/j.earscirev.2006.09.002.

Lustrino, M., Prelevic, D., Agostini, S., Gaeta, M., Di Rocco, T., Stagno, V., and Capizzi, L.S., 2016, Ca-rich carbonates associated with ultrabasic-ultramafic melts: Carbonatite or limestone xenoliths? A case study from the late Miocene Morron de Villamayor volcano (Calatrava Volcanic Field, central Spain): Geochimica et Cosmochimica Acta, v. 185, p. 477–497, https://doi.org/10.1016/j.gca.2016.02.026.

Madeira, J., Munhá, J., Tassinari, C.C.G., Mata, J., Brum da Silveira, A., and Martins, S., 2005, K/Ar ages of carbonatites from the island of Fogo (Cape Verde): VIII Congresso de Geoquimica dos Paises de Língua Portuguesa, v. 1, p. 475–478.

Mark, D.M., Barfod, D.N., Stuart, F.M., and Imlach, J., 2009, The ARGUS multi-collector noble gas mass spectrometer: Performance for ^{40}Ar/^{39}Ar geochronology: Geochemistry Geophysics Geosystems, v. 10, p. 1–13, https://doi.org/10.1029/2009GC002643.

Marks, M.A.W., Neukirchen, F., Vennemann, T., and Markl, G., 2009, Textural, chemical, and isotopic effects of late-magmatic carbonatitic fluids in the carbonatite-syenite Tamazeght complex, High Atlas Mountains, Morocco: Mineralogy and Petrology, v. 97, p. 23–42, https://doi.org/10.1007/s00710-009-0075-0.

Marzoli, A., Renne, P.R., Piccirilo, E.M., Ernesto, M., Bellieni, G., and DeMin, A., 1999, Extensive 200-million-year-old continental flood basalts of the Central Atlantic Magmatic Province: Science, v. 284, p. 616–618.

Mata, J., Alves, C.F., Martins, L., Miranda, R., Madeira, J., Pimentel, N., Martins, S., Azevedo, M.R., Youbi, N., De Min, A., Almeida, I.M., Bensalah, M.K., and Terrinha, P., 2015, ^{40}Ar/^{39}Ar ages and petrogenesis of the West Iberia Margin onshore magmatism at the Jurassic-Cretaceous transition: Geodynamic implications and assessment of open system processes involving saline materials: Lithos, v. 236–237, p. 156–172.

McDonough, W.F., and Sun, S., 1995, The composition of the Earth: Chemical Geology, v. 120, p. 223–253, https://doi.org/10.1016/0009-2541(94)00140-4.

McKenzie, D., and O'Nions, R.K., 1991, Partial melt distributions from inversion of rare earth element concentrations: Journal of Petrology, v. 32, p. 1021–1091, https://doi.org/10.1093/petrology/32.5.1021.

Melchiorre, M., Vergés, J., Fernández, M., Coltorti, M., Torne, M., and Casciello, E., 2017, Evidence for mantle heterogeneities in the westernmost Mediterranean from a statistical approach to volcanic petrology: Lithos, v. 276, p. 62–74, https://doi.org/10.1016/j.lithos.2016.11.018.

Menzies, M.A., Rogers, N., Tindle, A., and Hawkesworth, C.J., 1987, Metasomatic and enrichent processes in lithospheric peridotites, an effect of asthenosphere-lithosphere interaction, *in* Menzies, M.A., and Hawkesworth, C.J. eds., Mantle Metasomatism: London Academic Press Inc., p. 313–361.

Montero, P., Haissen, F., Mouttaqui, A., Molina, J.F., Errami, A., Sadki, O., Cambeses, A., and Bea, F., 2016, Contrasting SHRIMP U-Pb zircon ages of two carbonatite complexes from the pericratonic terranes of the Reguibat Shield: Implications for the lateral extension of the west African Craton: Gondwana Research, v. 38, p. 238–250, https://doi.org/10.1016/j.gr.2015.12.005.

Morishita, T., Hattori, K.H., Terada, K., Matsumoto, T., Yamamoto, K., Takebe, M., Ishida, Y., Tamura, A., and Arai, S., 2008, Geochemistry of apatite-rich layers in the Finero phlogopite-peridotite massif (Italian Western Alps) and ion microprobe dating of apatite: Chemical Geology, v. 251, p. 99–111, https://doi.org/10.1016/j.chemgeo.2008.02.018.

Muñoz, M., Sagredo, J., de Ignacio, C., Fernández-Suárez, J., and Jeffries, T.E., 2005, New data (U-Pb, K-Ar) on the geochronology of the alkaline-carbonatitic association of Fuerteventura, Canary Islands, Spain: Lithos, v. 85, p. 140–153, https://doi.org/10.1016/j.lithos.2005.03.024.

Nasir, S., and Rollinson, H., 2009, The nature of the subcontinental lithospheric mantle beneath the Arabian Shield: Mantle xenoliths from southern Syria: Precambrian Research, v. 172, p. 323–333, https://doi.org/10.1016/j.precamres.2009.05.004.

Neumann, E.R., 2004, The evolution of the upper mantle beneath the Canary Islands: Information from trace elements and Sr isotope ratios in minerals in mantle xenoliths: Journal of Petrology, v. 45, p. 2573–2612, https://doi.org/10.1093/petrology/egh063.

O'Reilly, S.Y., and Griffin, W.L., 2000, Apatite in the mantle: implications for metasomatic processes and high heat production in Phanerozoic mantle: Lithos, v. 53, p. 217–232.

O'Reilly, S.Y., and Griffin, W.L., 2013, Mantle metasomatism, *in* Harlov, D.E., and Austrheim, H., eds., Metasomatism and the chemical transformation of rock. The role of fluids in terrestrial and extraterrestrial processes: Lecture Notes in Earth System Sciences: Berlin, Springer-Verlag, p. 471–533, https://doi.org/10.1007/978-3-642-28394-9_12.

Paster, T.P., Schauwecker, D.S., and Haskin, L.A., 1974, The behaviour of some trace elements during solidification of the Skaergaard layered series: Geochimica et Cosmochimica Acta, v. 38, p. 1549–1577, https://doi.org/10.1016/0016-7037(74)90174-4.

Perfit, M.R., and Davidson, J.P., 2000, Plate tectonics and volcanism, *in* Sigurdsson, H., ed., Encyclopedia of Volcanoes: Academic Press, San Diego, p. 89–113.

Prowatke, S., and Klemme, S., 2006, Trace element partitioning between apatite and silicate melts: Geochimica et Cosmochimica Acta, v. 70, p. 4513–4527, https://doi.org/10.1016/j.gca.2006.06.162.

Raffone, N., Chazot, G., Pin, C., Vannucci, R., and Zanetti, A., 2009, Metasomatism in the lithospheric mantle beneath Middle Atlas (Morocco) and the origin of Fe- and Mg-rich wehrlites: Journal of Petrology, v. 50, p. 197–249, https://doi.org/10.1093/petrology/egn069.

Renne, P.R., Balco, G., Ludwig, K.R., Mundil, R., and Min, K., 2011, Joint determination of ^{40}K decay constants and ^{40}Ar/^{40}K for the Fish Canyon sanidine standard, and improved accuracy for ^{40}Ar/^{39}Ar geochronology [Reply]: Geochimica et Cosmochimica Acta, v. 75, p. 5097–5100, https://doi.org/10.1016/j.gca.2011.06.021.

Schettino, A., and Turco, E., 2011, Tectonic history of the western Tethys since the Late Triassic: Geological Society of America Bulletin, v. 123, p. 89–105, https://doi.org/10.1130/B30064.1.

Schmitz, M.D., and Kuiper, K.F., 2013, High-precision geochronology: Elements, v. 9, p. 25–30, https://doi.org/10.2113/gselements.9.1.25.

Schoene, B., and Bowring, S.A., 2006, U-Pb systematics of the McClure Mountain syenite: Thermochronological constraints on the age of the ^{40}Ar/^{39}Ar standard MMhb: Contributions to Mineralogy and Petrology, v. 151, p. 615–630, https://doi.org/10.1007/s00410-006-0077-4.

Sparks, R.S.J., Folkes, C.B., Humphreys, M.C.S., Barfod, D.N., Clavero, J., Sunagua, M.C., McNutt, S.R., and Pritchard, M.E., 2008, Uturuncu volcano, Bolivia: Volcanic unrest due to mid-crustal magma intrusion: American Journal of Science, v. 308, p. 727–769, https://doi.org/10.2475/06.2008.01.

Stoppa, F., and Sciazza, M., 2013, An overview of monogenetic carbonatitic magmatism from Uganda, Italy, China and Spain: Volcanologic and geochemical features: Journal of South American Earth Sciences, v. 41, p. 140–159, https://doi.org/10.1016/j.jsames.2012.10.004.

Stoppa, F., Rosatelli, G., Schiazza, M., and Tranquilli, A., 2012, Hydrovolcanic vs magmatic processes in forming maars and associated pyroclasts: the Calatrava-Spain-Case history, *in* Stoppa, F., ed., Updates in Volcanology—A comprehensive approach to volcanological problems: Tech-Open Access Publisher, p. 3–26.

Thomson, S.N., Gehrels, G.E., Ruiz, J., and Buchwaldt, R., 2012, Routine low-damage apatite U-Pb dating using laser ablation-multicollector-ICPMS: Geochemistry Geophysics Geosystems, v. 13, https://doi.org/10.1029/2011GC003928.

Thurner, S., Palomeras, I., Levander, A., Carbonell, R., and Lee, C.T., 2014, Ongoing lithospheric removal in the western Mediterranean: Evidence from Ps receiver functions and thermobarometry of Neogene basalts (PICASSO project): Geochemistry Geophysics Geosystems, v. 15, p. 1113–1127, https://doi.org/10.1002/2013GC005124.

Ubide, T., 2013, The Cretaceous alkaline magmatism in northeast Iberia. Igneous processes and geodynamic implications [Ph.D. thesis]: Universidad de Zaragoza, 223 p.

Ubide, T., Wijbrans, J.R., Galé, C., Arranz, E., Lago, M., and Larrea, P., 2014, Age of the cretaceous alkaline magmatism in northeast Iberia: Implications for the Alpine cycle in the Pyrenees: Tectonics, v. 33, p. 1444–1460, https://doi.org/10.1002/2013TC003511.

Villaseca, C., Ancochea, E., Orejana, D., and Jeffries, T.E., 2010, Composition and evolution of the lithospheric mantle in central Spain: Inferences from peridotite xenoliths from the Cenozoic Calatrava volcanic field, *in* Coltorti, M., Downes, H., Grégoire, M., and O'Reilly, S., eds., Petrological Evolution of the European Lithospheric Mantle: Geological Society, London, Special Publications 337, p. 125–151, https://doi.org/10.1144/SP337.7.

Wagner, C., Mokhtari, A., Deloule, E., and Chabaux, F., 2003, Carbonatite and alkaline magmatism in Taourirt (Morocco): Petrological, geochemical and Sr-Nd isotope characteristics: Journal of Petrology, v. 44, p. 937–965, https://doi.org/10.1093/petrology/44.5.937.

Wang, L.-X., Marks, M.A.W., Von Der Handt, A., Keller, J., Teiber, H., and Markl, G., 2014, Apatites from the Kaiserstuhl Volcanic Complex, Germany: New constraints on the relationship between carbonatite and associated silicate rocks: European Journal of Mineralogy, v. 26, p. 397–414.

Wartho, J.A., and Kelley, S.P., 2003, $^{40}Ar/^{39}Ar$ ages in mantle xenolith phlogopites: determining the ages of multiple lithospheric mantle events and diatreme ascent rates in southern Africa and Malaita, Solomon Islands: Geological Society, London, Special Publications, v. 220, p. 231–248, https://doi.org/10.1144/GSL.SP.2003.220.01.14.

Wilson, M., and Downes, H., 1991, Tertiary-Quaternary extension-related alkaline magmatism in Western and Central Europe: Journal of Petrology, v. 32, p. 811–849.

Yang, Y.H., Wu, F.Y., Wilde, S.A., Xliu, X.M., Zhang, Y.B., Xie, L.W., and Yang, J.H., 2009, *In situ* perovskite Sr-Nd isotopic constraints on the petrogenesis of the Ordovician Mengyin kimberlites in the North China craton: Chemical Geology, v. 264, p. 24–42, https://doi.org/10.1016/j.chemgeo.2009.02.011.

Zack, T., and Brumm, R., 1998, Ilmenite/liquid partition coefficients of 26 trace elements determined through ilmenite/clinopyroxene partitioning in garnet pyroxenite, *in* Gurney, J.J., Gurney, J.L., Pascoe, M.D., and Richardson, S.H., eds., 7th International Kimberlite Conference: Red Roof Design, Cape Town, p. 986–988.

Zangana, N.A., 1995, Geochemical variations in mantle xenoliths from Ray pic, Massif Central, France [PhD thesis]: University of London, 305 p.

Zheng, J., Griffin, W.L., O'Reilly, S.Y., Zhang, M., and Pearson, N., 2006, Zircons in mantle xenoliths record the Triassic Yangtze-North China continental collision: Earth and Planetary Science Letters, v. 247, p. 130–142, https://doi.org/10.1016/j.epsl.2006.05.011.

Zindler, A., and Hart, S.R., 1986, Chemical geodynamics: Annual Review of Earth and Planetary Sciences, v. 14, p. 493–571, https://doi.org/10.1146/annurev.ea.14.050186.002425.

MANUSCRIPT RECEIVED 17 JULY 2018
REVISED MANUSCRIPT RECEIVED 19 OCTOBER 2018
MANUSCRIPT ACCEPTED 4 DECEMBER 2018